RADIOCARBON SIMULATION FAILS TO SUPPORT THE SYNCHRONEITY REQUIREMENT OF THE YOUNGER DRYAS IMPACT HYPOTHESIS

Supplementary Data: Extended Methods and Alternative Simulations

Ian A. Jorgeson, Ryan P. Breslawski, Abigail E. Fisher

Contents

1. Detailed Description of Simulation Steps

The main text provides a general outline of the simulation, while this section describes the simulation steps in detail. A more detailed overview of the simulation can be obtained by downloading the R script and the comments contained within. Section 2 provides instructions for running this script.

The simulation is performed for a unique event, *E*. Here, *E* corresponds to either the hypothesized Younger Dryas Impact or the Laacher See volcanic eruption. For each event *E*, we performed the simulation for 10,000 iterations in each year $x_{E,i}$ in a vector x_E of calendar years. For the former event, we used dates corresponding to the purported Younger Dryas Boundary (YDB), and for the latter event we used dates associated with the Laacher See Tephra (LST). For the YDB, x_{YDB} spans 151 years within 12,860–12,710 cal yr BP, and for the LST, x_{LST} spans 151 years within 12,991–12,841 cal yr BP. The central 101 years in each x_E vector corresponds to a range of possible calendar years for each hypothesized event. We simulated over a 25-year buffer on each side of the hypothesized range to observe how expectations vary for calendar years proximate to the possible calendar years for each hypothesized event.

For each of the 10,000 iterations in each year $x_{E,i}$, the simulation performs four main steps:

(1) Create a vector of true calendar ages *C* for the synchronous event. The length of *C* depends on the number of ^{14}C measurements in the observed sample (30 for the YDB and 19 for the LST).
(2) Generate expected *target* ^{14}C values for each true calendar age C_i in vector *C*.
(3) For each *target* ^{14}C value, generate a *measured* ^{14}C value as observed by a laboratory.
(4) Calibrate each *measured* ^{14}C value with the IntCal13 ^{14}C calibration curve (Reimer et al., 2013).

The remainder of this section describes each of the four steps. These descriptions concern a single iteration for a single calendar age $x_{E,i}$. To help illustrate these steps, Table S1.1 provides a toy set of observed ^{14}C measurements that could be used as simulation input for a hypothetical synchronous event. We expand on this table with each simulation step. All references to "calendar ages/years/dates" indicate years BP (AD 1950). AMS refers to accelerator mass spectrometry, GPC refers to gas proportional counting, and LSC refers to liquid scintillation counting.

1.1. True Calendar Ages

For each iteration within calendar year $x_{E,i}$, a vector of repeated $x_{E,i}$ values is first generated. The length of this vector is determined by the number of measurements in the observed ^{14}C dataset. The YDB dataset consists of 30 reported dates, which creates a vector of 30 $x_{E,i}$ values for these simulations. The corresponding LST vector length is 19. For simulations that lack "old wood" effects, these repeated vectors are treated as the true calendar ages for each simulated ^{14}C measurement.

Some versions of the simulation account for "old wood" effects with an "old wood" model (OWM). These versions add a calendar year offset to each $x_{E,i}$ value. Additional years are added only to the $x_{E,i}$ values that correspond to dated materials from organisms that may have died prior to the event of interest. Twenty-four of 30 reported YDB measurements originate from such materials, and 18 of 19 reported LST measurements correspond to these materials. Short-lived samples, such as those from grasses or seeds, do not receive age offsets. The new vector of calendar years that includes offset values is referred to here as x_E^O (Table S1.2).

Table S1.1. A toy dataset of reported ^{14}C measurements for five samples associated with a hypothesized event E. These measurements were made by three laboratories with codes ABCD, EFGH, and IJKLM. The first and last laboratories measure ^{14}C via AMS, while EFGH measures ^{14}C via GPC. Three of the five measurements are on wood, indicating that they may correspond to calendar ages older than the event of interest. The simulation generates expected ^{14}C values (i.e., what might be observed in the μ column given a true synchronous event), while all other columns in this table provide context dependent input for the simulation itself.

	Reported ^{14}C			
Sample ID	**μ**	**σ**	**"old wood"?**	**Lab type**
ABCD-0001	10,251	25	No (seed)	AMS
ABCD-0002	10,290	35	No (seed)	AMS
EFGH-0001	10,295	75	Yes (wood)	GPC
EFGH-0003	10,299	55	Yes (wood)	GPC
IJKLM-0001	10,321	40	Yes (wood)	AMS

OWM age offsets are drawn randomly from an exponential distribution, with offset values near zero more likely. In other words, OWM offsets assume that organism death most likely occurred shortly before the calendar year of the event *E*, with the probability of an earlier death event decreasing with temporal distance from event *E*. We considered two exponential distributions, one with the λ parameter set to 0.04 and one with λ set to 0.01 (Figure S1.1). The former distribution is a conservative scenario in which old samples predate the event by few years (μ = 25, 95% HDI = 0–75), while the latter distribution results in larger age offsets on average (μ = 100, 95% HDI = 0–300; Figure S1.1b,c). New values are drawn from each exponential distribution for each of the 10,000 iterations, allowing for λ specific variability in "old wood" effects to be estimated across 10,000 iterations. These distributions were selected to bound the extremes of realistic offsets that might be expected given "old wood" effects.

Table S1.2. The initial step in a single simulation iteration. Here, the toy dataset is used as input for a simulation iteration at 12,000 cal yr BP. The reported ^{14}C means have been removed, as these do not serve as input for the simulation. The age offsets are shown for hypothetical values drawn from an exponential distribution with λ = 0.04.

	Reported ^{14}C					OWM	
Sample ID	**μ**	**σ**	**"old wood"?**	**Lab type**	$X_{E,i}$	**Offset**	$x_{E,i}^{O}$
ABCD-0001	-	25	No	AMS	12,000	N/A	12,000.00
ABCD-0002	-	35	No	AMS	12,000	N/A	12,000.00
EFGH-0001	-	75	Yes	GPC	12,000	27.5	12,027.50
EFGH-0003	-	55	Yes	GPC	12,000	6.10	12,006.10
IJKLM-0001	-	40	Yes	AMS	12,000	88.50	12,088.50

Most of the wood samples for Laacher See are *Populus* (Baales et al., 2002), which is most likely Eurasian aspen (*Populus tremula*) or black poplar (*Populus nigra*). The former species lives an average of 50–100 years (Caudullo and de Rigo, 2016) and can live up to 200 years (von Wühlisch, 2009). In contrast, black popular generally live only 20–50 years. As such, the conservative exponential model (λ = 0.04) generally gives offsets intermediate between the lifespans of these species (Figure S1.1b). The latter "old wood" exponential function (λ = 0.01) is more consistent with aspen and produces occasional offsets several centuries older than the lifespan of aspen (Figure S1.1c). This can accommodate scenarios in which dead wood on the landscape is incorporated into the geological stratum of interest. We assume that true "old wood" effects for the YDB and LST wood and charcoal ^{14}C samples fall somewhere between the two extremes defined by these exponential functions, and neither exponential function is intended to match precisely the "old wood" effects in either context, which are probably unknowable.

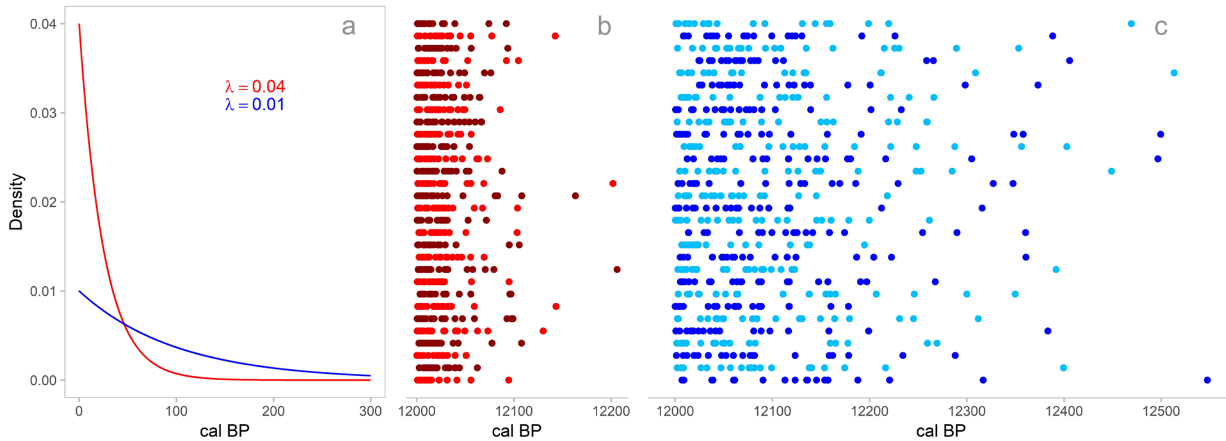

Figure S1.1. Exponential distributions used for versions of the simulation employing an OWM. (a) Probability density functions for each offset. (b and c) 30 examples of 20 "old wood" dates for a synchronous event at 12,000 cal yr BP, where each row is a sample of 20 dates. Panel b corresponds to an exponential distribution with λ = 0.04, and panel c corresponds to an exponential distribution with λ = 0.01.

1.2. Target ^{14}C Values

We generated a target ^{14}C value for each $x_{E,i}^{O}$ value in two steps. First, mean ^{14}C values were obtained by "uncalibrating" $x_{E,i}^{O}$ values with the uncalibrate function in the *rcarbon* R package (Bevan and Crema, 2018)**.** This function works by drawing from a normal distribution of ^{14}C values associated with a calendar year, where the distribution corresponds to the calibration curve error in the IntCal13 ^{14}C calibration curve (Figure S1.2a). This produces a hypothetical mean atmospheric ^{14}C value for the calendar year (Table S1.3). $x_{E,i}^{O}$ values that are identical receive the same uncalibrated mean atmospheric ^{14}C value since they correspond to a calendar year with the sample hypothetical mean atmospheric ^{14}C value. Mean atmospheric ^{14}C values are resampled for each of the 10,000 iterations.

Second, we account for intra-annual variability around the mean atmospheric ^{14}C value in a calendar year. We estimated the difference between seasonal extremes of atmospheric ^{14}C variability using data from McDonald et al. (2019). They estimate the distance between seasonal extremes of atmospheric ^{14}C with two calculation methods, each of which is performed for situations in which atmospheric ^{14}C production is in increasing and decreasing states (Table S1.4). We also consider stable atmospheric ^{14}C production, treated here as the midpoint between McDonald et al.'s (2019) values for increasing and decreasing production.

Table S1.3. The first part of step two for a single simulation iteration. Here, the toy dataset is used as input for a simulation iteration at 12,000 cal yr BP. The reported ^{14}C means have been removed, as these do not serve as simulation input. Mean atmospheric ^{14}C values have been sampled from the IntCal13 ^{14}C calibration curve error distribution around each calendar age $x_{E,i}^{O}$.

	Reported ^{14}C					
Sample ID	**μ**	**σ**	**"old wood"?**	**Lab type**	$x_{E,i}^{O}$	**Mean atmospheric ^{14}C**
ABCD-0001	-	25	No	AMS	12,000.00	10,222
ABCD-0002	-	35	No	AMS	12,000.00	10,222
EFGH-0001	-	75	Yes	GPC	12,027.50	10,261
EFGH-0003	-	55	Yes	GPC	12,006.10	10,300
IJKLM-0001	-	40	Yes	AMS	12,088.50	10,366

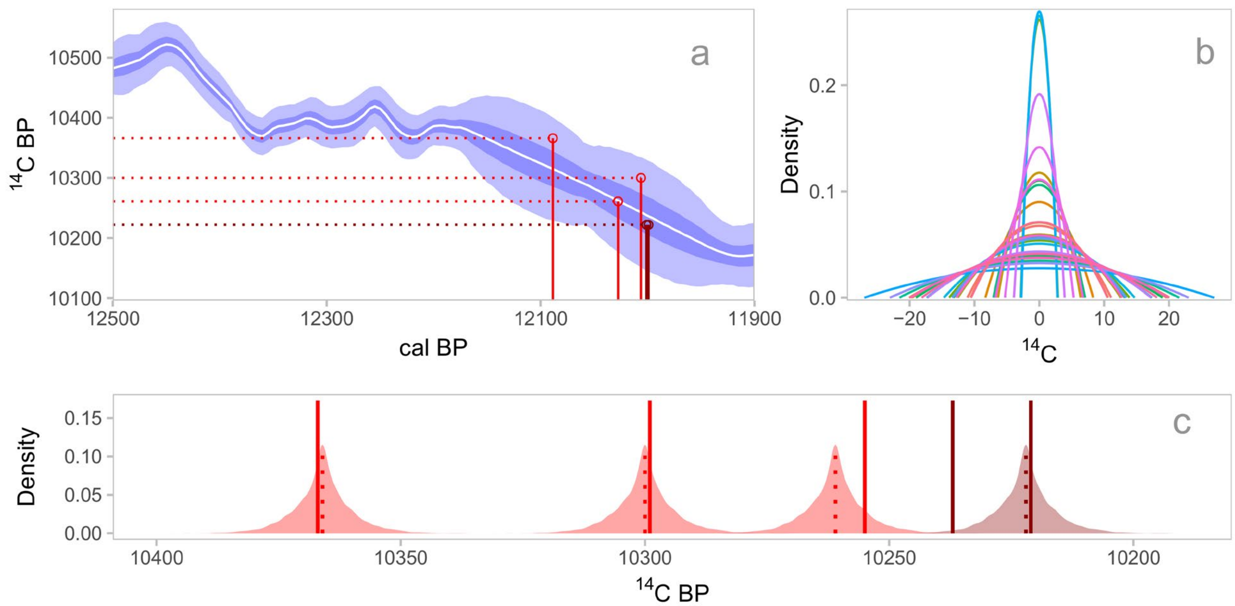

Figure S1.2. A visual schematic of simulated target ^{14}C values based on context dependent input from the toy dataset: (a) "Uncalibrating" five calendar ages (i.e., converting $x_{E,i}^{O}$ values into mean atmospheric ^{14}C values; Table S1.3 for details). The blue calibration curve bands show the 50% and 95% error regions, and the white line shows the mean value of the curve. (b) 30 randomly sampled beta distributions that represent possible intra-annual distributions of ^{14}C variability. (c) Mean "uncalibrated" ^{14}C values (dotted lines), intra-annual ^{14}C variability around those values based on 10,000 randomly sampled beta distributions (red semitransparent regions), and ^{14}C values sampled from those intra-annual ^{14}C variability distributions (solid lines). The ^{14}C values sampled from each intra-annual distribution comprise the target ^{14}C values. These are the values that laboratories attempt to measure. In panels a and c, light red geometry corresponds to three calendar ages with "old wood" effects, and dark red geometry corresponds to two overlapping calendar ages that date the event of interest.

Table S1.4. Estimates of the intra-annual distance between atmospheric ^{14}C extremes (McDonald et al., 2019 for increasing and decreasing values. The stable values are the midpoints between the increasing and decreasing values).

Intra-annual distance	Error	Atmospheric ^{14}C trend	Calculation method
18.0	13.0	Increasing	First
23.0	16.0	Decreasing	First
20.5	14.5	Stable	First
26.0	16.0	Increasing	Second
22.0	13.0	Decreasing	Second
24.0	14.5	Stable	Second

To estimate intra-annual atmospheric ^{14}C variability, we first modelled possible values as sparsely beta distributed β(2, 2), centered on 0, and scaled by the intra-annual distance. Since the intra-annual distance is imprecisely known, we simulated 10,000 beta distributions scaled by samples drawn from N(Intra-annual distance, Error) (Figure S1.2b). For each of the 10,000 samples, we randomly selected one of the six possible distance and error pairings. Therefore, these distributions average across atmospheric ^{14}C production trends and calculation methods. For each of the 10,000 simulation iterations, a random value is drawn from one of the 10,000 centered and scaled beta distributions. This random value is then added to the mean atmospheric ^{14}C value to estimate a target ^{14}C value that reflects both inter- and intra-annual ^{14}C variability (Table S1.5; Figure S1.2c).

Table S1.5. The second part of step two for a single simulation iteration. Here, the toy dataset is used as input for a simulation iteration at 12,000 cal yr BP. The reported ^{14}C means have been removed, as these do not serve as input for the simulation.

	Reported ^{14}C		"old	Lab	Mean	Intra-annual	
Sample ID	μ	σ	wood"?	type	atmospheric ^{14}C	variation offset	Target ^{14}C
ABCD-0001	-	25	No	AMS	10,222	15	10,237
ABCD-0002	-	35	No	AMS	10,222	-1	10,221
EFGH-0001	-	75	Yes	GPC	10,261	-6	10,255
EFGH-0003	-	55	Yes	GPC	10,300	-1	10,299
IJKLM-0001	-	40	Yes	AMS	10,366	1	10,367

1.3. Measured ^{14}C Values

Given minor inter-laboratory variability that conditions systematic biases, as well as minor instrumental error that shapes intra-laboratory measurement repeatability, measured ^{14}C values depart from their target values (Boaretto et al., 2003; International Study Group, 1982; Scott et al., 1990, 1998, 2010a; Scott, Cook, and Naysmith, 2007). As such, the dispersion of reported ^{14}C values should vary based on the number of laboratories that have contributed to a reported ^{14}C dataset, as well as based on laboratory specific characteristics that might further influence the repeatability of measurements. These sources of inter- and intra-laboratory variability can be used to model expected departures of ^{14}C measurements from their target values, given known numbers of laboratories and measurements per laboratory.

To estimate this variability, we fit a Bayesian multilevel model to data reported in the Fifth International Radiocarbon Intercomparison (VIRI) (Scott et al., 2010a, 2010b; Scott, Cook, Naysmith et al., 2007). We refer to this model as the Laboratory Measurement Bias and

Repeatability Model, or LBM. The LBM treats ^{14}C measurements as a normally distributed outcome. We defined a three-parameter linear model for the outcome mean: a categorical intercept for each sample material, a random categorical effect for laboratory ID, and a scaling parameter that adjusts the random laboratory ID effect based on whether the laboratory performs AMS or GPC/LSC measurements. We defined a four-parameter linear model for the outcome standard deviation. Parameters consist of a baseline intercept, a random categorical effect for laboratory ID, a linear effect for reported measurement error, and a categorical effect that accounts for whether laboratories perform AMS or GPC/LSC measurements. Section 3 describes this model in detail, including the model formula, prior distributions for model parameters, and a posterior predictive check.

The simulation samples 10,000 sets of values from the posterior distributions of the LBM parameters, with a unique set of parameter values applied to each of the 10,000 simulation iterations (Figure S1.3). Therefore, uncertainty in the model parameters is distributed across iterations within each calendar year $x_{E,i}$:

1. A random offset from the target ^{14}C value representing the mean observed value within each laboratory. The number of sampled offsets is determined by the number of laboratories that contributed to the reported ^{14}C dataset (Table S1.6).
2. A multiplier term that rescales the offset for GPC/LSC laboratories (Table S1.6).
3. A random within-laboratory standard deviation that is rescaled by an additional multiplier value for GPC/LSC laboratories (σ_L). This standard deviation further varies by the error reported for each ^{14}C measurement (Table S1.7).
4. Values are then drawn from laboratory and sample specific distributions defined by N(Mean laboratory specific ^{14}C, σ_L), representing ^{14}C values that might be measured by each laboratory (Table S1.8).

The standard deviation for expected within lab measured ^{14}C variability depends on the reported error of the sample (σ). It takes the form,

$$\sigma_L = exp(Lab\ effect + GPCLSC\ effect + log\ (\sigma) * \sigma\ effect) * 100.01.$$

(Equation S1.1)

Possible values for each effect are presented in Table S1.7. The 100.01 value to the right of the exponential transformation puts the result on the scale of ^{14}C years (the LBM is fitted to ^{14}C year z-scores, and therefore, the output of this linear model needs to be put back on the ^{14}C year scale).

The measured ^{14}C values comprise an expected set of observations generated for a single iteration. The simulation records the standard deviation of these values, $\sigma^{14}C$ (69.80 for the toy dataset detailed here), as an expected measure of dispersion for a series of ^{14}C measurements, given a synchronous event. This is completed over 10,000 iterations for each calendar year $x_{E,i}$, yielding a distribution of simulated $\sigma^{14}C$ values given the number of labs, lab types (AMS or GPC/LSC), reported measurement errors, and potential “old wood” effects associated with a reported ^{14}C dataset. For versions of the simulation that exclude the LBM, these $\sigma^{14}C$ values are calculated with the target ^{14}C values rather than the measured ^{14}C values (as calculated in Step 2).

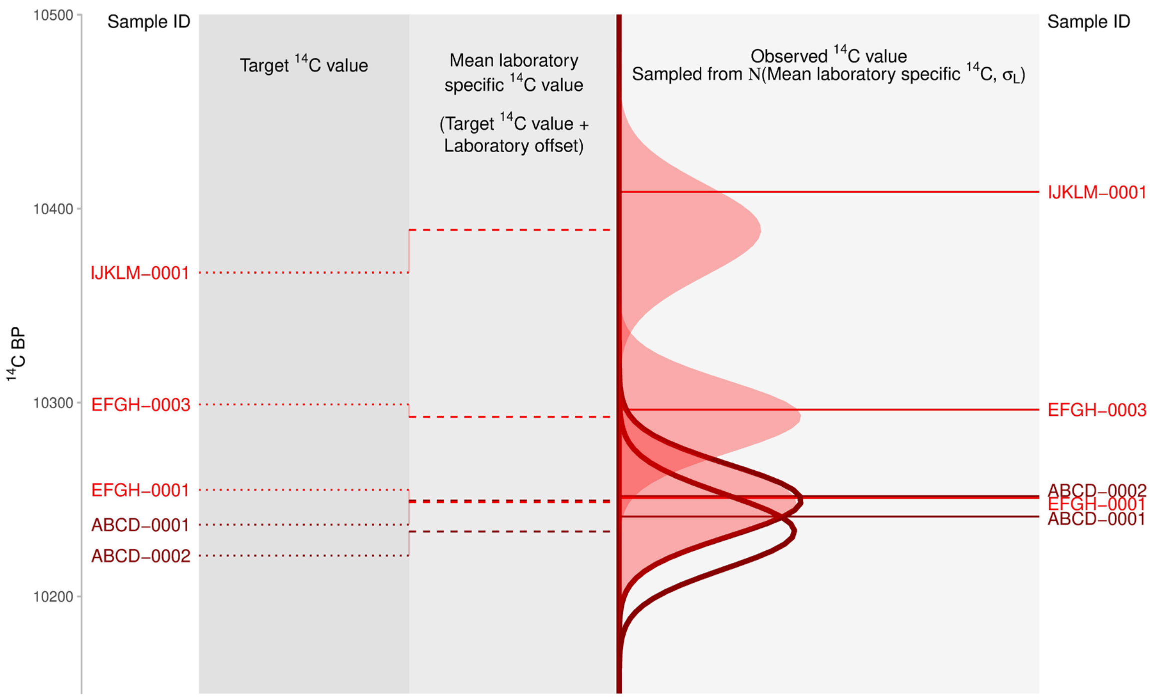

Figure S1.3. An example of five target ^{14}C values being converted to measured ^{14}C values via sampling from the LBM. Refer to Tables S1.6, S1.7, and S1.8 for the values depicted in this figure. Light red lines correspond to three calendar ages with "old wood" effects, and dark red lines correspond to two calendar ages that date the event of interest. Rotated normal distributions illustrate intra-laboratory sampling distributions for each measured ^{14}C value; They correspond to the distribution of repeated measurements for a given laboratory at a given reported measurement error, centered on the mean laboratory specific ^{14}C value for a target ^{14}C value. Two normal distributions with empty fills and dark red outlines depict calendar ages that lack "old wood" effects, and three normal distributions with light red fills and no outlines show calendar ages with "old wood" effects. Note, the intra-laboratory sampling distributions for ABCD-0001 and EFGH-0001 overlap nearly completely, and the values sampled for ABCD-002 and EFGH-0001 are very similar.

Table S1.6. Obtaining mean laboratory offset values for measured ^{14}C in a single simulation iteration. Here, the toy dataset is used as input for a simulation iteration at 12,000 cal yr BP. The reported ^{14}C means have been removed, as these do not serve as input for the simulation. The laboratory offset and GPC/LSC multiplier values are sampled from the LBM parameters, which vary across the 10,000 simulation iterations.

	Reported ^{14}C						
Sample ID	**μ**	**σ**	**Lab type**	**Target ^{14}C**	**Lab offset**	**GPC|LSC multiplier**	**Mean lab specific ^{14}C**
ABCD-0001	-	25	AMS	10,237	12.50	N/A	10,249.50
ABCD-0002	-	35	AMS	10,221	12.50	N/A	10,233.50
EFGH-0001	-	75	GPC	10,255	-5.80	1.1	10,248.60
EFGH-0003	-	55	GPC	10,299	-5.80	1.1	10,292.60
IJKLM-0001	-	40	AMS	10,367	22.00	N/A	10,389.00

Table S1.7. Parameters for sampling measured ^{14}C values. Here, the toy dataset is used as input for a simulation iteration at 12,000 cal yr BP. The reported ^{14}C means have been removed, as these do not serve as input for the simulation. Laboratory effects, GPC/LSC effects, and σ effects are sampled from the posterior distributions of the LBM parameters, which vary across the 10,000 simulation iterations.

	Reported ^{14}C		Lab	Mean lab	Within lab std. deviation (σ_L) parameters		
Sample ID	**μ**	**σ**	**type**	**specific ^{14}C**	**Lab effect**	**GPC|LSC effect**	**σ effect**
ABCD-0001	-	25	AMS	10,249.50	-2.10	0	0.35
ABCD-0002	-	35	AMS	10,233.50	-2.10	0	0.35
EFGH-0001	-	75	GPC	10,248.60	-2.50	0.32	0.35
EFGH-0003	-	55	GPC	10,292.60	-2.50	0.32	0.35
IJKLM-0001	-	40	AMS	10,389.00	-1.90	0	0.35

Table S1.8. Sampled measured ^{14}C values. Here, the toy dataset is used as input for a simulation iteration at 12,000 cal yr BP. The reported means have been removed, as these do not serve as input for the simulation. Lab/sample deviations were calculated with the "Within lab std. deviation parameters" from Table S1.7 using Equation S1.1.

	Reported ^{14}C		Lab	Within lab sampling parameters		Measured ^{14}C
Sample ID	**μ**	**σ**	**type**	**^{14}C μ**	**Std. deviation (σ_L)**	**value**
ABCD-0001	-	25	AMS	10,249.50	18.40	10,241.20
ABCD-0002	-	35	AMS	10,233.50	19.10	10,251.70
EFGH-0001	-	75	GPC	10,248.60	18.90	10,250.80
EFGH-0003	-	55	GPC	10,292.60	18.40	10,296.30
IJKLM-0001	-	40	AMS	10,389.00	23.60	10,408.60

1.4. Calibrated ^{14}C Measurements

The simulation then calibrates the measured ^{14}C values using the errors described in the reported dataset, producing a probability density across calendar ages for each measurement (Table S1.9; Figure S1.4). This is accomplished with the IntCal13 curve using the calibrate function in the *rcarbon* R package (Bevan and Crema, 2018).

Table S1.9. Sampled measured ^{14}C values and the 95% highest density intervals (HDI) for their calibrated age densities. Here, the toy dataset is used as input for a simulation iteration at 12,000 cal yr BP. The reported means have been removed, as these do not serve as input for the simulation. Note that the measured ^{14}C values in the simulation are calibrated with σ values for the reported measurements.

	Reported ^{14}C		Measured ^{14}C		
Sample ID	**μ**	**σ**	**μ**	**σ**	**Cal yr BP (95% HDIs)**
ABCD-0001	-	25	10,241.20	25	12,111–11,921; 11,915–11,827
ABCD-0002	-	35	10,251.70	35	12,130–11,826
EFGH-0001	-	75	10,250.80	75	12,384–12,264; 12,246–11,711
EFGH-0003	-	55	10,296.30	55	12,386–12,262; 12,249–11,929; 11,894–11,829
IJKLM-0001	-	40	10,408.60	40	12,517–12,482; 12,424–12,085

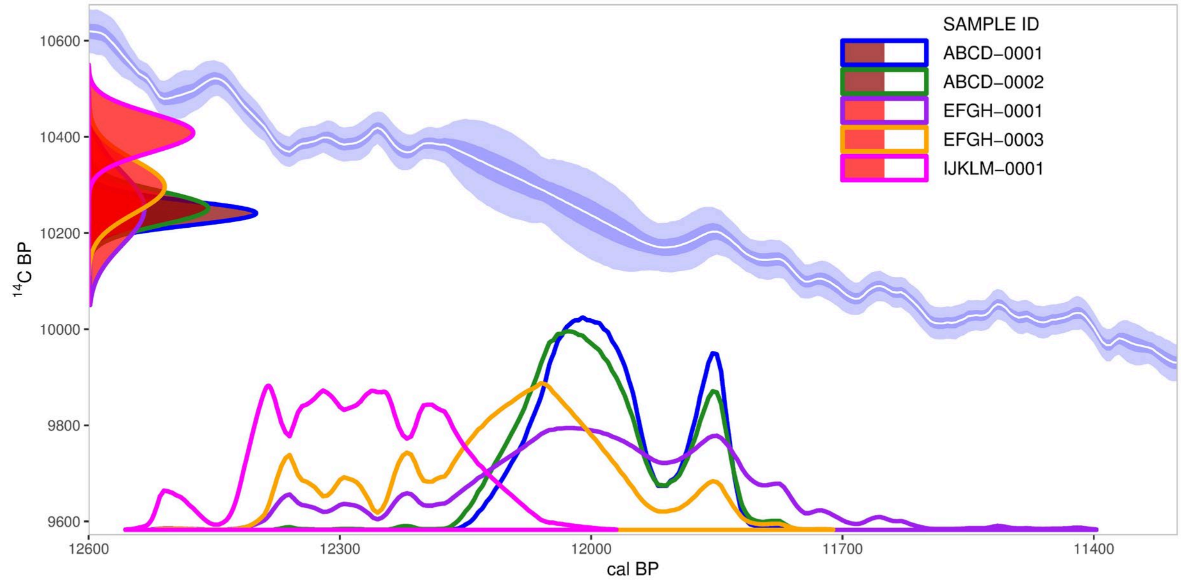

Figure S1.4. Toy dataset: Five simulated ^{14}C measurements (rotated normal distributions) calibrated with the IntCal13 calibration curve (white line with blue bands). The blue calibration curve bands show the 50% and 95% error regions and the white line depicts the mean curve value. Light red geometry corresponds to three samples with "old wood" effects, and dark red geometry corresponds to two overlapping samples that date the event of interest. The undulating distributions on the x-axis depict calibrated age densities, which are used to calculate dissimilarity values.

Following calibration, dissimilarity values are then obtained by first calculating the Manhattan distance between each pair of age densities (Table S1.10):

$$Manhattan\ distance = \sum_{i=1}^{c} \left| A_{x,i} - A_{y,i} \right|,$$

(Equation S1.2)

where $A_{x,i}$ indexes the proportion of age density A_x in calendar year i, $A_{y,i}$ indexes the proportion of age density A_y in calendar year i, and c is the length of a vector defined by the union of calendar ages shared by the pair of age densities. The expected dissimilarity value is then calculated by taking the mean of all pairwise Manhattan distances and dividing this mean by two. A value of exactly zero indicates that the age densities are identical, while a value of exactly one indicates that the set of age densities are completely nonoverlapping. Like the $\sigma^{14}C$ values calculated at the end of Step 3, 10,000 dissimilarity values are obtained for each year $x_{E,i}$ across the iterations.

Table S1.10. Manhattan distances between each pair of the five calibrated age distributions in the toy dataset. The mean of these values is divided by two to obtain a measure of dissimilarity (0.508 for this toy dataset). Here, the toy dataset is used as input for a simulation iteration at 12,000 cal yr BP.

	ABCD-001	**ABCD-002**	**EFGH-001**	**EFGH-003**	**IJKLM-001**
ABCD-001					
ABCD-002	0.19				
EFGH-001	0.71	0.62			
EFGH-003	0.95	0.80	0.63		
IJKLM-001	1.86	1.81	1.48	1.14	

2. Guide to Running the Simulation

This simulation consists of an R script that is designed to run on a cluster. Parallelization occurs across the range of 302 simulated years (151 years each for the LST and the YDB). Optimally, one year is assigned per available core, plus one additional core for the master process. If at least one core is available per year, execution time is mainly limited by the number of simulation iterations. The results in this paper were obtained by executing the R script on the ManeFrame II cluster at Southern Methodist University (SMU), utilizing one core per simulated year. Under these circumstances, a 10,000-iteration simulation completes in about 36 hours, a 1000-iteration simulation completes in just under four hours, and 100 iterations completes in about 0.5 hours. Simulations under 1000 iterations generally provide noisy output distributions of $\sigma^{14}C$ and dissimilarity values. If cores are limited and multiple years are run per core, execution time will increase dramatically depending on the core that is assigned the most years over which to simulate (henceforth, maximum-core-years). Estimated execution time is roughly maximum-core-years multiplied by the above specified time estimates. For example, if maximum-core-years is three for a 10,000-iteration simulation on the ManeFrame II cluster, the expected time is 3*36 hours.

2.1. Requirements

Stan: The LBM is fit via Hamiltonian Monte Carlo simulation in Stan (Stan Development Team, 2018). Visit https://www.mc-stan.org for installation details.

R packages: *rstan* (Stan Development Team, 2018), *ggplot2* (Wickham, 2016), *parallel* (R Core Team, 2018), *reshape2* (Wickham, 2007), *rcarbon* (Bevan and Crema, 2018), *matrixStats* (Bengtsson et al., 2018), *patchwork* (Pedersen, 2018), and *rethinking (*McElreath, 2017). The first six packages are available in the CRAN.
patchwork is available at: https://github.com/thomasp85/patchwork
rethinking is available at: https://github.com/rmcelreath/rethinking

Data files: *IRI.csv* (table of reported ^{14}C measurements from the Fifth International Radiocarbon Intercomparison), *RCmeasurements.csv* (table of dates reported for the Laacher See Tephra and Younger Dryas Boundary).

The script must be executed on a cluster with cores distributed across nodes. The main file output (*SimDat#.RData*) for the 10,000-iteration simulation is 587 MB, and there are minor memory spikes during the simulation (intermediate R objects are created during the simulation that are not included in the main output file).

2.2. Running the R Script

Place the R script, *IRI.csv*, and *RCmeasurements.csv* in your working directory. Ensure that Stan and all required R packages are installed. Follow these steps:

1. Adjust user-arguments for simulation. Navigate to the 'USER ARGUMENTS' block of code in the R script to adjust the simulation as appropriate (code lines ~220-305). This block contains variables that specify the number of nodes to be used, the number of cores per node, the number of simulation iterations, plotting options, the ranges of calendar years over which to simulate each event, OWM parameter values, and other variables of interest. Inline code comments further detail each variable.
2. Source the R script. This will load the csv data files and prepare parameters for the simulation. On the first run, the script fits the LBM, which may take 5-15 minutes. After the

model is fitted, posterior parameter values are exported in RData file *IRI#.RData* (where '#' is the number of user-specified iterations for the simulation). If you leave this file in your working directory and you plan to run the simulation again in the future, the script will read *IRI#.RData* into the simulation rather than refit the model, saving run time. Every time a simulation is run with a new number of iterations (i.e., new '#' values), the model will be refitted. As such, users can store multiple *IRI#.RData* files for running the simulation with different numbers of iterations. The correct file will be read automatically for each simulation if it has already been generated in the working directory.

3. <u>Monitor the working directory for intermediate output files</u>. In addition to *IRI#.RData*, the script will output *SimDatIntermediate.RData*. This file contains simulation parameters to be read by each node. If you wish to delete this file, do not so until the simulation has initiated on every node (i.e., every node has imported the simulation parameters from *SimDatIntermediate.RData*). Immediately following the creation of *SimDatIntermediate .RData*, the main R script will create daughter R script files with the filename *NodeSim#.R*. The number of these scripts that is created corresponds to the number of user-specified nodes. After these scripts appear in the working directory, move to Step 4.

4. <u>Submit daughter scripts to the cluster</u>. The main R script also outputs an sbatch array submit script that can be executed to request nodes for every daughter R script (*nodesim.sh*). This is formatted to run on the ManeFrame II cluster at SMU, but it can be easily edited to run on other clusters using a Slurm workload manager. Alternatively, you may submit the daughter scripts to nodes using your own method.

5. <u>Wait for results</u>. After you submit the daughter scripts, the main R script waits for them to complete (it scans the working directory every 30 seconds for output from the daughter scripts). When a daughter script completes, it outputs *NodeDat#.RData*. After all daughter output files are present in the working directory, the main script automatically imports them, aggregates the results, and creates one output RData file (*SimDat#.RData*, where '#' is the number of user specified simulation iterations).

2.3. Results and Output Files

Simulation results are contained in objects stored in *SimDat#.RData*. Comments in the script describe these objects. This file is automatically written to the working directory after the simulation completes. *SimDat#.RData* can be opened and explored in an interactive R session on a personal computer**.** Although the intermediate output files may be of interest (*IRI#.RData*, *SimDatIntermediate.RData*, *NodeDat#.RData*, *NodeSim#.R*, and *nodesim.sh*), they do not contain the primary results and may be deleted after the simulation is completed.

3. Laboratory Measurement Bias and Repeatability Model (LBM)

This section has four parts: (1) a description of the Fifth International Radiocarbon Intercomparison (VIRI) dataset to which the LBM was fitted, (2) model formulas and prior distributions for parameters, (3) a description of the posterior parameter values, and (4) a description of Hamiltonian Monte Carlo (HMC) diagnostics with a posterior predictive check. The goal of this model is to estimate parameters that describe inter-lab variation in the measurement of the ^{14}C content of a sample as well as intra-laboratory variation over repeated measurements of a sample. This involves estimating the distributions of mean ^{14}C values and ^{14}C standard deviations across laboratories.

3.1. The VIRI Dataset

To fit the model, we first aggregated data presented in the VIRI (Scott et al., 2010a, 2010b; Scott, Cook, Naysmith et al. 2007). These data included all ^{14}C measurements across all sample materials for which ^{14}C measurements were reported (samples B, D, F, G, H, and I). In total, this spans 420 measurements performed by 80 laboratories.

We transformed these data in three steps. First, we centered all ^{14}C measurements on the median value for each sample material. Second, we used these centered measurements to investigate the presence of outliers. Outliers were conservatively defined as measurements that fall at least six times the interquartile range (IQR) distance outside the first and third quartile within each set of ^{14}C measurements for a sample material. The values identified as outliers may have resulted from unusually poor quality-control for some laboratories or from other anomalies in measurement. After outliers were identified, all measurements associated with the laboratory that produced an outlier were removed from the dataset (Figure S3.1). This reduced the number of laboratories from 80 to 68, and the number of ^{14}C measurements from 420 to 361. Finally, these median-centered measurements were converted to z-scores (Figure S3.1).

3.2. Model Formula and Prior Distributions for Parameters

Each of the 361 median-centered ^{14}C z-scores is associated with four additional variables: a categorical sample material ID (B, D, F, G, H, or I), a categorical laboratory ID, a dummy variable indicating whether than laboratory performed an AMS (0) or GPC/LSC measurement (1), and the reported measurement errors for ^{14}C values. Although measurement errors should represent uncertainty in the reported means, laboratories calculate these errors in a variety of ways that may not be comparable (Scott, Cook, and Naysmith, 2007). As such, we treat them as predictor variables for the dispersion of reported ^{14}C means, with the expectation that within-laboratory ^{14}C measurement dispersion increases with larger reported errors.

First, we defined the likelihood for median-centered ^{14}C z-scores as

$$^{14}C \sim N(\mu, \sigma).$$

(Equation S3.1)

Median-centered ^{14}C z-scores are distributed N(μ, σ). We then modelled μ as a linear outcome of the ^{14}C value of sample material i, C_s[sample i], and an offset from that sample material value that depends on the laboratory ID, C_o[lab j]. The laboratory ID offset also varies based on the AMS vs GPC/LSC dummy variable, AMS, through parameter C_{AMS}:

$$\mu = C_s[sample\ i] + C_O[lab\ j] \times (1 + (C_{AMS} - 1) \times AMS).$$

(Equation S3.2)

Since median-centered ^{14}C z-scores likely approximate a true sample-specific value near zero, we use a prior distribution of N(0, 1) for each C_s[sample i]. We modelled C_o[lab j] as distributed N(0, C_O^{σ}), with the prior for C_O^{σ} set to exp(2). C_{AMS} may reduce or increase the effect of C_o[lab j], but it does not affect the sign of C_o[lab j], taking only positive values. Values less than 1 reduce the lab specific offset C_o[lab j], while values greater than 1 increase the lab specific offset C_o[lab j]. As such, for C_{AMS} we use a gamma distribution with the mean centered on 1 as a prior: gamma(1, 0.5). The parameterization of this prior does not follow the base *dgamma* R function, but instead uses the *dgamma2* parameterization included in the *rethinking* R package (McElreath, 2017).

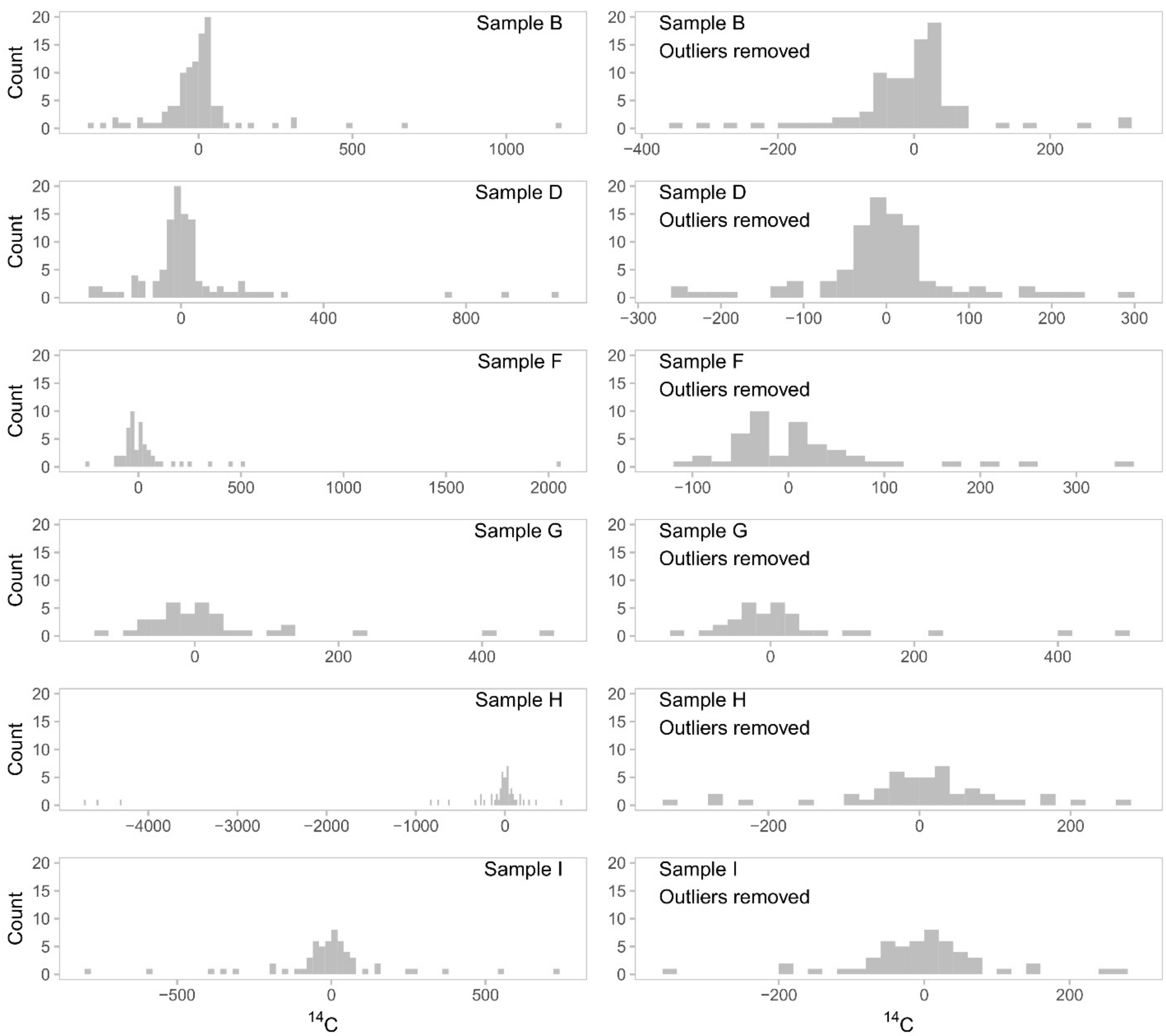

Figure S3.1. Histograms of median-centered ^{14}C z-scores for samples B, D, F, G, H, and I. Left panels show all available measurements (n = 420), and right panels show only those measurements that originate from laboratories that did not produce outlier values (n = 361). The values in the right panels were used to fit the LBM.

σ can then be interpreted as intra-laboratory variation in median-centered ^{14}C z-scores. We modelled σ as the linear outcome of a baseline parameter shared by all laboratories, σ_l, a laboratory ID specific offset parameter, σ_{lab}[lab j], the log reported measurement error (log(ME)) multiplied by parameter σ_{ME}, and a parameter that is expressed only for GPC/LSC laboratories (σ_{AMS}). As such, the dispersion of repeated intra-laboratory ^{14}C z-scores depends on laboratory specific variation in repeatability, the reported measurement error associated with those measurements, and whether the measurement was obtained via AMS or GPC/LSC. Laboratory specific variation depends on each reported ^{14}C measurement error, which can vary from value to value within a single laboratory. To constrain σ on the positive scale, we used a log link function:

$$log(\sigma) = \sigma_{lab}[lab\ j] + \sigma_l + \sigma_{ME} \times log(ME) + \sigma_{AMS} \times AMS.$$

(Equation S3.3)

We assigned the same informative normal prior distribution to σ_l, σ_l, and σ_{AMS}: N(0, 1). We modelled σ_{lab}[lab j] as distributed N(0, $\sigma_{lab}{}^{\sigma}$), with the prior for $\sigma_{lab}{}^{\sigma}$ set to exp(2). Readers may note that we have not modelled covariance between the random laboratory parameters, C_o[lab j] and σ_{lab}[lab j]. For the simulation, the practical implication of this decision is that these parameter values are sampled independently for simulated laboratories rather than from a multivariate distribution. Such covariance is often modelled as multivariate normal, which would be inappropriate here, as σ_{lab} should vary with only the magnitude of C_O rather than the magnitude and sign of C_O (i.e., a parabolic rather than monotonic relationship). In other words, we might expect within-laboratory dispersion to vary with absolute laboratory ID offset, regardless of whether the laboratory ID offset is above or below the target ^{14}C value (Figure S3.2). For the sake of model simplicity and interpretability, we did not attempt to model a parabolic relationship between these parameters.

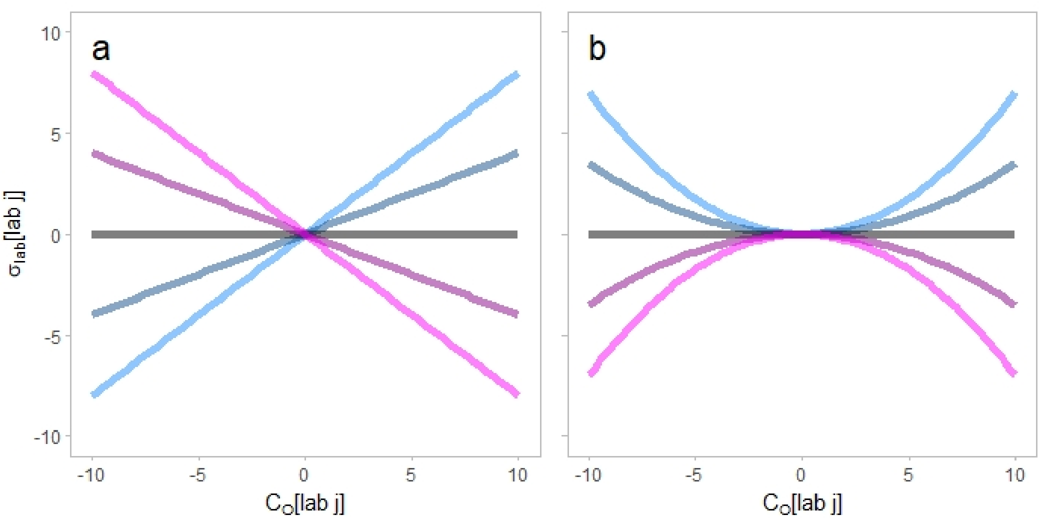

Figure S3.2. (a) Example relationships that might be expected if laboratory parameters covaried monotonically. (b) Example relationships that might be expected given a parabolic relationship between parameters. Given the lack of a covariance component in the model, laboratory parameters were estimated independently, conforming to the horizontal grey relationship in each panel (i.e., no covariance).

This model assumes that systematic offsets between mean laboratory measurements and target ^{14}C values are maintained across any sample materials that a laboratory might measure. For example, consider a laboratory faced with measuring three different sample materials: A, B, and C. If the laboratory takes measurements that are on-average -10 ^{14}C years from the target value of sample A, this mean offset will be also be present when the same laboratory measures the ^{14}C values of sample materials B and C. If the systematic offset varies between sample materials A, B, and C, this cannot be captured by the model. This model also assumes that within-laboratory repeatability is uniform across sample materials A, B, and C. In reality, different sample material types (e.g., bone, wood, grass seeds) and variability in target ^{14}C values may affect both systematic offsets and within-laboratory repeatability. Unfortunately, the available VIRI dataset is insufficient to explore these issues in detail with this model.

The LBM was specified using the *map2stan* function in the *rethinking* R package (McElreath, 2017) and fitted through Hamiltonian Monte Carlo (HMC) simulation in *rstan* (Stan Development Team, 2018). The model was fitted with four chains, each of which performed 5000 warmup and 2500 sampling iterations (10,000 total sampling iterations).

3.3. Posterior Parameter Values

Posterior estimates for each sample material ^{14}C value are close to each material's observed sample median (Figure S3.3a). Each posterior distribution for these sample materials includes its respective observed median value in a high-density region (since sample values are median centered, the observed median value is 0 for each distribution). The posterior distribution for C_{AMS} has a mean of 1.26, indicating that GPC/LSC laboratories generally have larger mean offsets from target ^{14}C values than do AMS laboratories (Figure S3.3b). However, this posterior is fairly dispersed, with 36.6% of the distribution falling below 1. Values below 1 correspond to a scenario where GPC/LSC laboratories have smaller mean offsets than those mean offsets associated with AMS laboratories.

The modelled laboratory offset parameters, C_O[lab i], have mean posterior parameter values ranging from -29.0 to 26.3 ^{14}C years across the 68 laboratories (Table S3.1; Figure S3.4a). These posteriors show high overlap. At first glance, laboratory offset posteriors appear to show that between-laboratory variability is much higher than within-laboratory variability (Figure S3.4). However, this is only in the hypothetical scenario where a laboratory reports 0 measurement error. When measurement error is included, modelled within laboratory σ values increase rapidly and exceed the mean laboratory offsets (Figure S3.5; Figure S3.3e).

Posterior distributions for σ parameters are expressed on the log scale (Figure S3.5c–e). The posterior for the global parameter for σ, σ_l, has a mean value of 2.8 when this distribution is exponentiated and transformed back into the scale of ^{14}C years (95% HPDI: 0.7–5.6). This represents within-laboratory measurement repeatability for the average AMS laboratory when reported ^{14}C measurement error is zero. When σ_{lab} distributions are added to this average value, within-laboratory repeatability varies between laboratories. For the 68 labs in this dataset, the mean posterior σ value ranges from 1.53 to 9.92 ^{14}C years (Table S3.1). However, these posterior distributions are dispersed and show considerable overlap. In general, the effect of σ_{AMS} causes GPC/LSC laboratories to have higher within-laboratory variability than AMS laboratories (Figure S3.3d; Figure S3.4b; Figure S3.5).

The generative aspect of this model allows one to simulate hypothetical pairs of laboratory parameters (Figure S3.6). As expected, GPC/LSC laboratories have generally larger mean offsets and within-laboratory σ values than AMS laboratories.

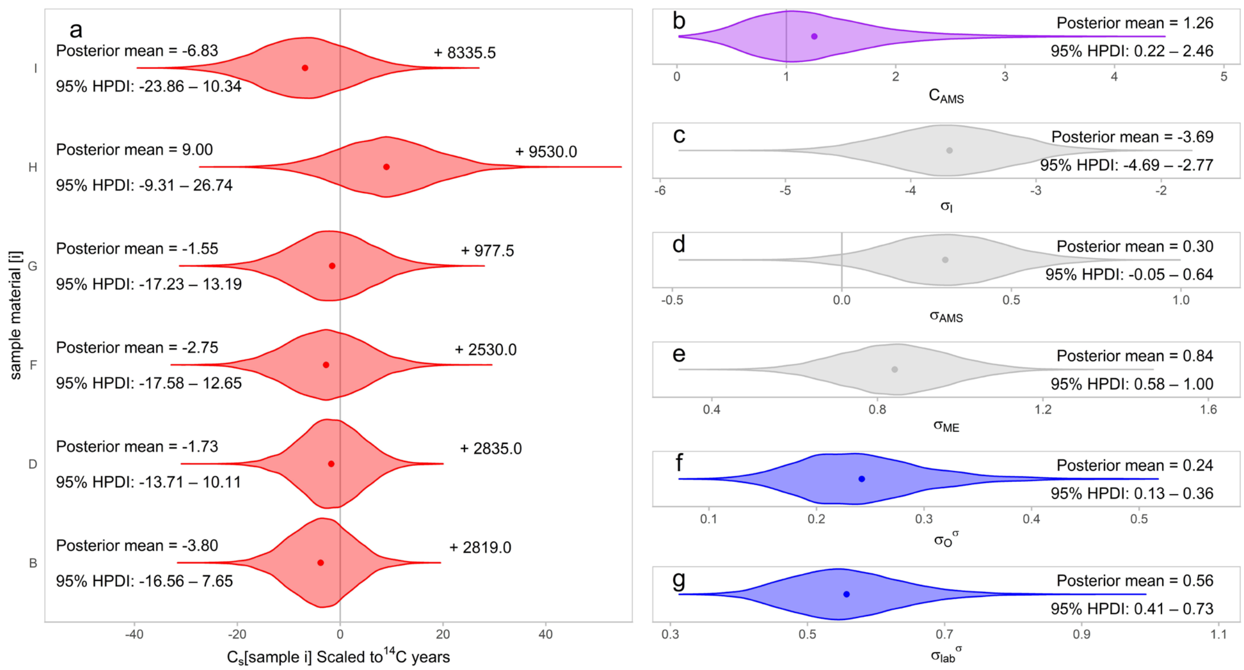

Figure S3.3. Posterior densities, posterior means (dots), and 95% highest posterior density intervals (HPDI) for model parameters. (a) Posteriors for each median-centered sample material. The sample medians are displayed to the right of each density to indicate over which ^{14}C years the non-centered distributions fall. (b) Posterior distribution for C_{AMS}, which adjusts mean laboratory offsets if they are GPC/LSC measurements. Note, most of the density sits above 1, indicating that GPC/LSC laboratory offsets are probably more dispersed than their AMS counterparts. (c–d) Posterior distributions for the standard deviation parameters (σ_I, σ_{AMS}, and σ_{ME}), which are displayed on the log scale. (f–g) Posterior distributions for the standard deviations of the distributions of each laboratory specific parameter, σ_O^σ and σ_{lab}^σ (i.e., mean laboratory-specific offsets and laboratory-specific standard deviations).

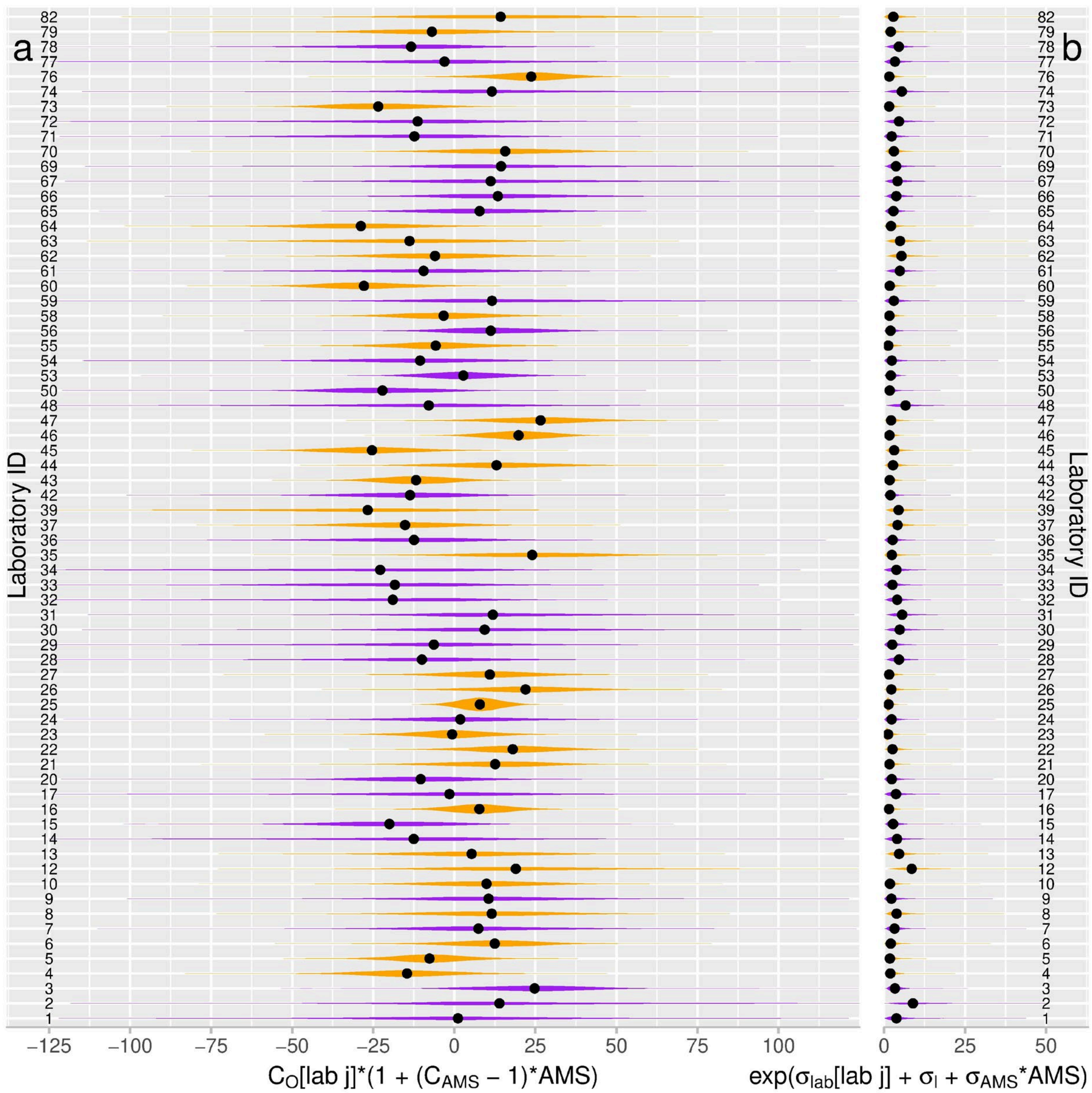

Figure S3.4. Posterior distributions for (a) mean laboratory offsets and (b) within-laboratory standard deviations. Gold densities show AMS laboratories and purple densities show GPC/LSC laboratories. GPC/LSC effects on laboratory offsets and within laboratory standard deviation values are included in these posterior distributions. Black dots mark the medians of each distribution. Note, within-laboratory standard deviations (b) assume 0 reported measurement error, and, in practice, these values become larger (see Figure S3.5). X-axes are on the ^{14}C year scale.

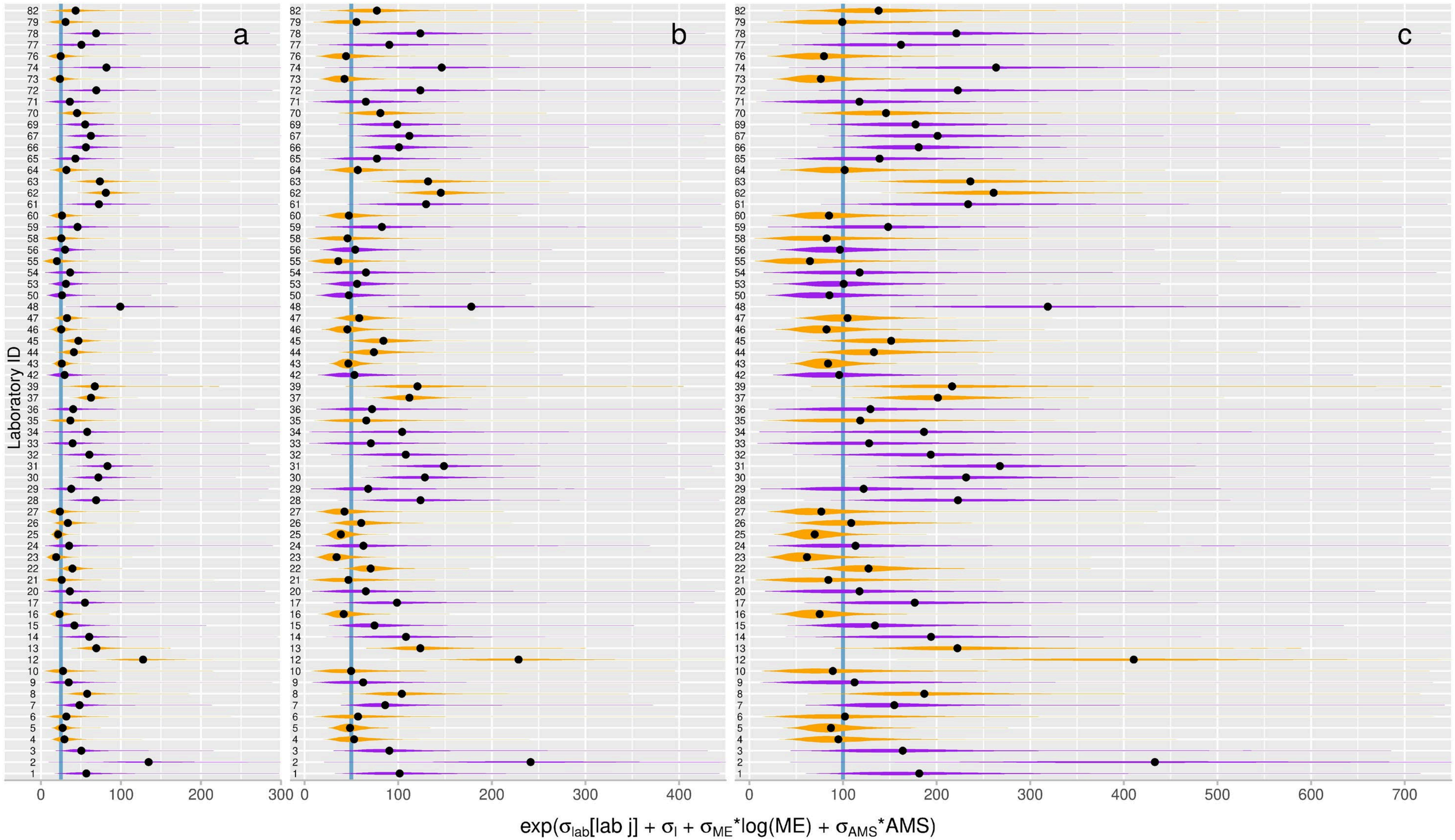

Figure S3.5. Three examples showing how reported measurement error (ME) affects within-laboratory standard deviations: (a) ME = 25 ^{14}C years, (b) ME = 50 ^{14}C years, and (c) ME = 100 ^{14}C years. Vertical blue lines mark the reported error values. Gold posterior densities are AMS laboratories and purple posterior densities are GPC/LSC laboratories. Black dots mark median values in each posterior density. GPC/LSC effects on within-laboratory standard deviations are included in these posterior distributions. X-axes are on the ^{14}C year scale.

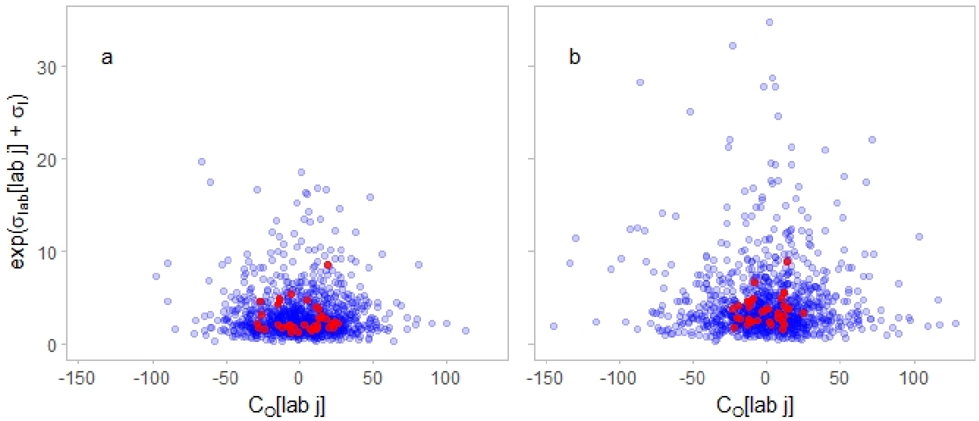

Figure S3.6. Laboratory parameters for (a) AMS and (b) GPC/LSC laboratories. Blue dots show 1000 simulated laboratories and red dots show mean posterior values for laboratories in the VIRI dataset. Both axes are displayed on the ^{14}C year scale.

Table S3.1. Posterior means and 95% highest posterior density intervals (HPDI) for VIRI laboratory parameters. The effects of GPC/LSC measurement methods are excluded here. In other words, all laboratories are treated here as AMS laboratories to express variability that is due to laboratory identity exclusive of ^{14}C measurement method.

Lab. ID [j]	Laboratory mean offset (^{14}C years) C_O[lab j]		Intra-laboratory standard deviation (^{14}C years) $\exp(\sigma_{lab}[\text{lab j}] + \sigma_l)$	
1	1.27	(-48.45 – 47.78)	3.54	(0.41 – 8.77)
2	14.87	(-38.29 – 71.87)	7.89	(1.44 – 17.99)
3	21.31	(-8.09 – 56.94)	2.88	(0.65 – 6.11)
4	-14.20	(-42.09 – 13.91)	2.32	(0.47 – 5.08)
5	-7.52	(-29.32 – 14.78)	2.09	(0.47 – 4.42)
6	11.97	(-18.54 – 41.52)	2.62	(0.41 – 6.40)
7	7.09	(-31.19 – 49.82)	2.85	(0.48 – 6.37)
8	11.62	(-25.75 – 47.68)	4.54	(0.94 – 9.87)
9	8.95	(-30.30 – 49.86)	2.18	(0.24 – 5.52)
10	9.47	(-27.11 – 45.79)	2.32	(0.25 – 5.59)
12	21.16	(-27.98 – 77.48)	9.92	(2.11 – 21.35)
13	5.61	(-31.05 – 41.74)	5.30	(1.25 – 11.18)
14	-12.61	(-65.43 – 37.58)	3.70	(0.53 – 8.91)
15	-16.92	(-52.35 – 17.87)	2.44	(0.42 – 5.30)
16	7.74	(-10.95 – 26.83)	1.82	(0.35 – 3.92)
17	-1.70	(-51.05 – 46.33)	3.49	(0.41 – 8.72)
20	-8.79	(-44.27 – 26.74)	2.24	(0.19 – 5.50)
21	11.63	(-24.49 – 43.44)	2.19	(0.18 – 5.57)
22	18.04	(-6.20 – 42.05)	3.03	(0.76 – 6.40)
23	-0.60	(-23.73 – 22.72)	1.53	(0.24 – 3.42)
24	2.00	(-38.73 – 45.11)	2.21	(0.20 – 5.35)
25	7.93	(-4.37 – 20.12)	1.60	(0.49 – 3.10)
26	21.80	(-8.74 – 50.63)	2.65	(0.58 – 5.81)
27	10.90	(-17.98 – 41.21)	1.92	(0.37 – 4.29)

28	-9.63	(-58.45 – 39.77)	4.14	(0.78 – 9.69)
29	-6.62	(-55.05 – 43.62)	2.42	(0.22 – 6.21)
30	9.20	(-35.61 – 55.32)	4.28	(0.69 – 9.66)
31	11.28	(-33.59 – 57.48)	4.85	(0.84 – 10.67)
32	-18.65	(-73.86 – 29.13)	3.62	(0.47 – 8.45)
33	-15.23	(-59.45 – 28.70)	2.42	(0.27 – 6.03)
34	-21.21	(-73.84 – 29.64)	3.47	(0.30 – 8.31)
35	23.47	(-17.02 – 63.13)	3.03	(0.33 – 7.25)
36	-10.87	(-54.42 – 29.74)	2.47	(0.33 – 6.01)
37	-15.38	(-45.41 – 15.47)	4.73	(1.16 – 9.54)
39	-29.02	(-84.32 – 20.78)	5.36	(0.81 – 11.78)
42	-11.70	(-46.12 – 24.47)	1.80	(0.26 – 4.24)
43	-11.68	(-32.10 – 9.40)	2.02	(0.44 – 4.22)
44	13.21	(-20.36 – 44.39)	3.24	(0.59 – 7.06)
45	-25.20	(-52.19 – 2.26)	3.59	(0.82 – 7.41)
46	19.72	(-0.37 – 39.30)	1.95	(0.45 – 4.03)
47	26.32	(-1.93 – 52.93)	2.53	(0.53 – 5.38)
48	-8.16	(-59.22 – 40.86)	5.93	(0.94 – 13.58)
50	-18.49	(-51.68 – 12.90)	1.58	(0.20 – 3.61)
53	2.49	(-21.70 – 24.94)	1.82	(0.34 – 3.93)
54	-8.95	(-48.71 – 30.48)	2.26	(0.25 – 5.58)
55	-5.29	(-34.24 – 22.08)	1.67	(0.14 – 4.15)
56	9.84	(-21.37 – 39.56)	1.79	(0.30 – 4.04)
58	-3.11	(-32.11 – 28.43)	2.14	(0.17 – 5.16)
59	11.95	(-35.21 – 61.90)	2.84	(0.29 – 6.99)
60	-26.96	(-53.13 – 0.31)	2.10	(0.37 – 4.65)
61	-9.55	(-58.01 – 39.37)	4.40	(0.62 – 10.24)
62	-6.03	(-38.43 – 26.03)	6.26	(1.31 – 13.27)
63	-14.42	(-60.64 – 27.33)	5.83	(1.07 – 12.76)
64	-28.35	(-60.61 – 6.38)	2.55	(0.44 – 5.71)
65	6.83	(-29.71 – 45.51)	2.62	(0.35 – 6.23)
66	13.15	(-21.49 – 52.30)	3.26	(0.54 – 7.00)
67	10.71	(-34.82 – 57.40)	3.77	(0.62 – 8.79)
69	13.29	(-30.11 – 60.55)	3.29	(0.50 – 7.46)
70	15.81	(-17.36 – 51.36)	3.53	(0.74 – 7.60)
71	-11.08	(-55.76 – 34.09)	2.24	(0.22 – 5.64)
72	-12.08	(-65.29 – 41.20)	4.21	(0.56 – 10.05)
73	-22.75	(-50.96 – 6.54)	1.92	(0.28 – 4.38)
74	12.59	(-38.32 – 67.89)	4.98	(0.68 – 11.78)
76	23.24	(0.83 – 44.15)	1.98	(0.34 – 4.50)
77	-3.51	(-51.84 – 47.22)	3.24	(0.34 – 8.18)
78	-13.89	(-60.91 – 29.29)	4.11	(0.60 – 9.37)
79	-6.77	(-42.76 – 29.40)	2.61	(0.32 – 6.37)
82	15.92	(-33.75 – 69.33)	3.67	(0.40 – 9.18)

3.4. HMC Diagnostics and Posterior Predictive Checks

To ensure convergence of HMC chains, we examined trace plots, R-hat values, and effective sample sizes. Trace plots indicate convergence of HMC chains for all parameters. All R-hat values are below 1.01. Effective sample sizes close to 10,000 indicate efficient sampling of posterior parameter spaces. Of the 148 parameters, 101 have effective sample sizes of 10,000. The median effective sample size is also 10,000, the mean is 8362, and the minimum is 1056.4 (Figure S3.7).

We also performed a posterior predictive check by simulating data from the model and plotting these simulated data against the VIRI ^{14}C measurements (Figure S3.8). For simplicity, where a laboratory contributed multiple ^{14}C measurements for a given sample material, we used the average reported measurement error for that laboratory ID and sample (for example, laboratories 5 and 22 in the panel for Sample G). In all but nine of the 361 VIRI ^{14}C measurements (97.5%), the 95% prediction intervals overlap the observed values. This indicates that the LBM does a reasonable job recovering the observed values.

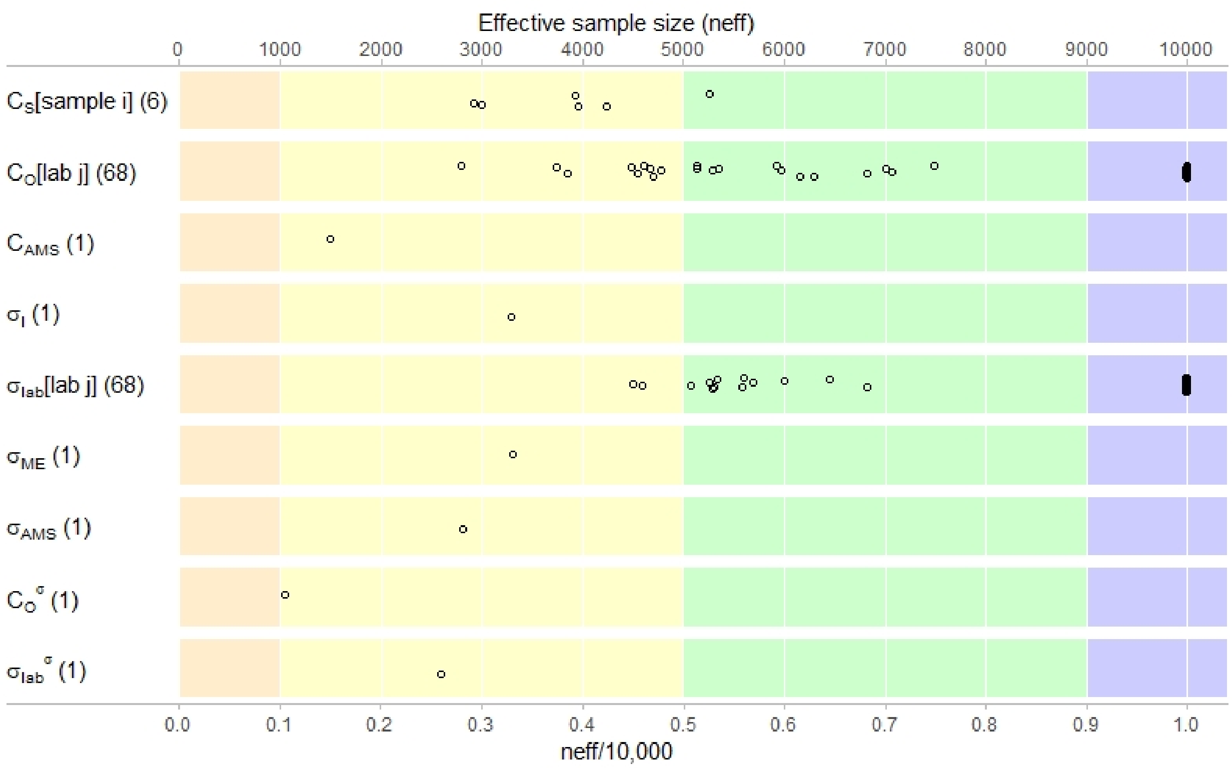

Figure S3.7. Distribution of effective sample sizes across parameters. Parenthetical values show the number of parameter distributions that were sampled for each parameter type.

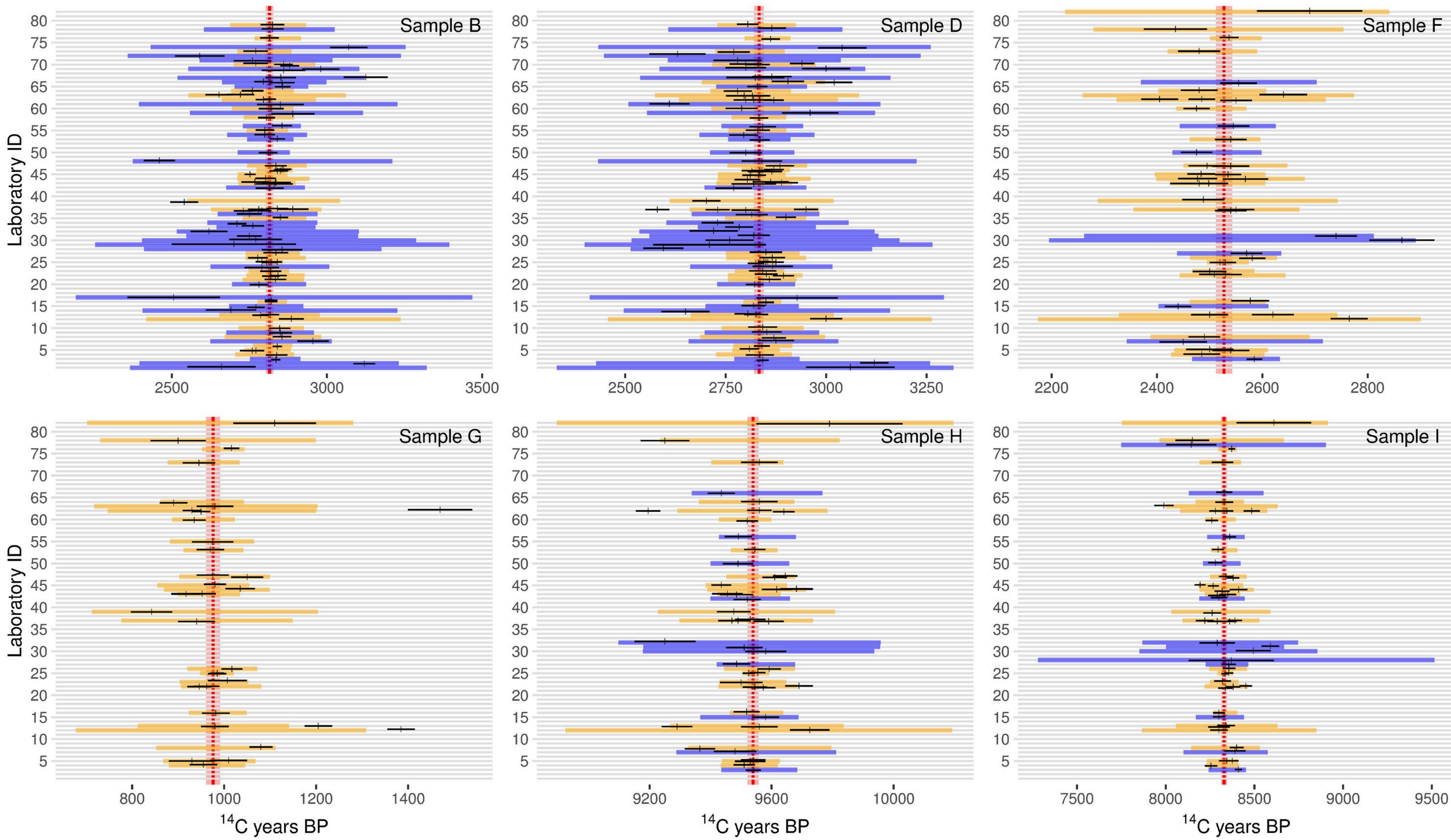

Figure S3.8. Posterior predictive check for the LBM. Each panel is a sample material reported in the VIRI study (Scott et al. 2010a,b; Scott, Cook, Naysmith et al., 2007). Laboratory IDs are listed along the y-axes. Reported ^{14}C measurements and their associated errors (1 σ) are indicated by vertical and horizontal black segments, respectively. Horizontal gold and purple bars show the 95% posterior prediction intervals for AMS and GPC/LSC laboratories, respectively. The dashed red lines and bands indicate the mean and 95% highest posterior density intervals for the ^{14}C value of each sample material.

4. Site and ^{14}C Sample Selection for the YDB and LST

Our simulations included only those ^{14}C measurements that are associated with samples from materials located within the YDB or LST stratigraphic layers. In this section, we list the sites with ^{14}C measurements taken on samples from these layers and describe those samples. Where applicable, we detail why certain sites or samples were excluded from the simulations.

4.1. YDB Sites and ^{14}C Samples

We compiled a preliminary list of ^{14}C measurements for the YDB based on those samples that Kennett et al. (2015) present as originating from within a YDB layer. From there, we assessed each primary source to ensure the accuracy of each measurement and its provenience. The table below outlines the decisions made for each sample. Two samples that Kennett et al. (2015) identified as originating from the YDB, yet were excluded in our simulations, are described in rows highlighted in orange. Twenty-one rows highlighted in blue describe samples that other publications describe as associated with a YDB layer while Kennett et al. (2015) indicate otherwise. We did not include these samples in our simulations.

Lab Number	Reported ^{14}C		Material	References
	μ	σ		
Abu Hureyra, Syria				
UCIAMS-105429	11,070	40	Charcoal	Bunch et al., 2012; Wittke et al., 2013
OxA-172	10,900	200	Charred Seed	Bunch et al., 2012; Moore et al., 2000; Wittke et al., 2013
OxA-430	11,020	150	Charred bone	Bunch et al., 2012; Moore et al., 2000; Wittke et al., 2013
OxA-468	11,090	150	Charred bone	Bunch et al., 2012; Moore et al., 2000; Wittke et al., 2013
BM-1718R	11,140	140	Charcoal	Bunch et al., 2012; Moore et al., 2000; Wittke et al., 2013
Discussion				
UCIAMS-105429 is the only sample that Kennett et al. (2015) report as directly associated with the YDB layer at Abu Hureyra. However, Wittke et al. (2013) indicate that this sample is not associated with the YDB layer. Sample OxA-172 (Moore et al., 2000) was originally interpreted by Wittke et al. (2013) as being located within the YDB layer at Abu Hureyra. However, Kennett et al. (2015, SI8) state that OxA-172 is "adjacent" to sample UCIAMS-105429, but not within the YDB layer. We default to Kennett et al. (2015) regarding the provenience of these samples and have included sample UCIAMS-105429 but not sample OxA-172 in our simulations. Bunch et al. (2012) identified samples OxA-430, OxA-468, and BM-1718R as close to the YDB layer via an age-depth model, although it is not clear that these samples were located within the YDB layer. Given their unsecure spatial relationship to the Abu Hureyra YDB layer, we deferred to Wittke et al. (2013) and Kennett et al. (2015) and excluded these samples from our simulations.				
Arlington Canyon, California, United States				
UCIAMS-47239	11,105	30	Charcoal	Kennett et al., 2008
UCIAMS-36308	11,095	25	Wood	Kennett et al., 2008
UCIAMS-42816	11,095	25	Wood	Kennett et al., 2008
UCIAMS-36307	11,070	25	Wood	Kennett et al., 2008
UCIAMS-36961	11,440	90	Carbon elongate	Kennett et al., 2008
UCIAMS-36960	11,185	30	Carbon spherule	Kennett et al., 2008
UCIAMS-36962	11,110	35	Wood	Kennett et al., 2008
UCIAMS-36959	11,075	30	Glassy carbon	Kennett et al., 2008
Beta-161032	10,860	70	Charcoal	Kennett et al., 2008
UCIAMS-36306	11,375	25	Wood	Kennett et al., 2008

UCIAMS-36305	11,235	25	Wood	Kennett et al., 2008
UCIAMS-36304	11,105	30	Wood	Kennett et al., 2008
Discussion				
Kennett et al. (2015) indicate that all 12 of these samples are associated with the YDB at Arlington Canyon. We have included all 12 measurements in our simulations.				
Barber Creek, North Carolina, United States				
No sources report ^{14}C measurements on samples recovered from the YDB layer.				
Big Eddy, Missouri, United States				
AA-27486	11,900	80	Charcoal	Hajic et al., 2007
AA-26654	10,710	85	Charcoal	Lopinot et al., 1998; Wittke et al., 2013
AA-25778	10,260	85	Wood charcoal	Hajic et al., 2007
AA-72612	10,959	54	Charcoal	Lopinot et al., 2000; Wittke et al., 2013
Discussion				
Kennett et al. (2015) designated two samples as associated with the YDB, AA-27486 and AA-26654. Wittke et al. (2013) identified a peak in nanodiamonds between 327 and 335 cm below surface, leading Kennett et al. (2015) to differentiate samples within these depths from samples taken at other depths within the same stratum. In contrast, Hajic et al. (Hajic et al., 2007) do not distinguish these two samples from an additional four samples within that stratum. Although located within the YDB layer, Kennett et al. (2015) rejected AA-25778 as an outlier based on an OxCal age-sequence model and we have thus excluded it from our simulations. Wittke et al. (2013) identify AA-72612 as associated with the YDB, although Kennett et al. (2015) indicate that this sample is from a context stratigraphically above the YDB. We excluded AA-72612 from our simulations.				
Blackwater Draw, New Mexico, United States				
SMU-1880	10,780	110	Soil humate	Johnson and Holliday, 1997; Wittke et al., 2013
Discussion				
Wittke et al. (2013) report that sample SMU-1880 is located within the YDB at Blackwater Draw (measurement originally reported by Johnson & Holliday (1997)). However, Kennett et al. (2015) do not include this sample in their narrative description, figures, or tables. Their supplemental OxCal code indicates that this sample was incorporated into an age-sequence model as a potential outlier. No other potential YDB samples are reported in the literature. Since Kennett et al. (2015) do not explicitly identify SMU-1880 as associated with the YDB, we do not include this measurement in our simulations.				
Blackville, South Carolina, United States				
No sources report ^{14}C measurements on samples recovered from the YDB layer.				
Bull Creek, Oklahoma, United States				
Beta-184854	11,070	60	Sediment organics	Bement et al., 2014
Discussion				
Bement et al. (2014) identified a Late Holocene peak in nanodiamonds not associated with the YDB.				
Daisy Cave, California, United States				
No sources report ^{14}C measurements on samples recovered from the YDB layer.				
Geldrop-Aalsterhut (Aalsterhut), Netherlands				
GrA-49524	10,840	75	Charcoal	van Hoesel et al., 2012
GrA-49509	10,865	55	Charcoal	van Hoesel et al., 2012
GrA-49515	11,020	75	Charcoal	van Hoesel et al., 2012
GrA-49570	10,735	45	Charcoal	van Hoesel et al., 2012
GrA-49521	10,765	50	Charcoal	van Hoesel et al., 2012
GrA-49516	10,765	50	Charcoal	van Hoesel et al., 2012
GrA-49507	10,920	50	Charcoal	van Hoesel et al., 2012
GrA-49527	10,960	60	Charcoal	van Hoesel et al., 2012
GrA-49529	10,755	55	Charcoal	van Hoesel et al., 2012
GrA-49573	10,860	45	Charcoal	van Hoesel et al., 2012

GrA-49574	10,845	45	Charcoal	van Hoesel et al., 2012
GrA-49569	10,895	45	Charcoal	van Hoesel et al., 2012
GrA-49514	10,880	110	Charcoal	van Hoesel et al., 2012
GrA-49575	10,900	50	Charcoal	van Hoesel et al., 2012
Discussion				
van Hoesel et al. (2012) report 14 ^{14}C sample measurements from the charcoal-rich Usselo Horizon, which they identify as a stratigraphic marker with the potential to evaluate the Younger Dryas Impact hypothesis. Kennett et al. (2015) exclude 11 of these sample measurements on the basis that they originate from the upper portion of the Usselo Horizon, which does not have nanodiamond markers. In their OxCal age-sequence model, Kennett et al. (2015) placed these three YDB samples stratigraphically below the remaining 11 samples. In our simulations, we only included ^{14}C measurements from these three samples.				
Indian Creek, Montana, United States				
No sources report ^{14}C measurements on samples recovered from the YDB layer.				
Lake Cuitzeo, Michoacán, Mexico				
No sources report ^{14}C measurements on samples recovered from the YDB layer.				
Lake Hind, Manitoba, Canada				
UCIAMS-29317	10,610	25	Charcoal	Firestone et al., 2007
Discussion				
Kennett et al. (2015) indicate that the single YDB ^{14}C sample is located below a peat layer, citing Firestone et al. (2007). Firestone et al. (2007), however, do not describe the sample used for the ^{14}C measurement. Firestone et al. (2007) describe black mats, microspherules, glass-like carbon, and magnetic grains associated with the YDB, but they do not describe the context of the sample.				
Lindenmeier, Colorado, United States				
I-141	10,780	135	Charcoal	Haynes and Agogino, 1960; Kinzie et al., 2014; Walton et al., 1961
Discussion				
Kinzie et al. (2014) state that there were no ^{14}C samples obtained from the nanodiamond rich layer that they define as the YDB. They indicate that sample I-141 is stratigraphically directly above the YDB (Kinzie et al., 2014). We follow Kennett et al. (2015), who indicate that this sample dates the YDB layer, and have included it in our simulations. I-141 was first published as 10,780±375 ^{14}C yr BP (Haynes and Agogino, 1960) and later corrected to 10,780±135 ^{14}C yr BP (Walton et al., 1961). Like Kennett et al. (2015), we use the corrected error term.				
Lingen, Lower Saxony, Germany				
Beta-369246	10,870	40	Charcoal	Kennett et al., 2015
Discussion				
Wittke et al. (2013) identify the YDB layer at 42–45cmbs by an abundance of charcoal combined with the presence of impact-related spherules. Kennett et al. (2015) rely on this identification for their association of this sample with the YDB.				
Lommel, Belgium				
UCIAMS-46303	11,480	100	Charcoal	Wittke et al., 2013
N/A	10,950	50	N/A	van Geel et al., 1989; Wittke et al., 2013
Discussion				
Kennett et al. (2015) do not identify any ^{14}C samples from within the YDB, conflicting with a previous publication. Wittke et al. (2013) report an AMS measurement on charcoal from the Lommel YDB layer (UCIAMS-46303). They also include an AMS measurement on charcoal of 10,950±50 ^{14}C yr BP, although it lacks provenience information or a laboratory ID (Wittke et al., 2013). Wittke et al. (2013) cite van Geel et al. (1989) as the source for this measurement. However, van Geel et al. (1989) appear to have estimated the ^{14}C age of the onset of the Younger Dryas rather than report a ^{14}C measurement on a sample material. This likely explains why this value is not associated with a provenience or laboratory ID, it is not a ^{14}C measurement. Kennett et al. (2015) indicate that UCIAMS-46303 is stratigraphically below the YDB, and they do not include the latter ^{14}C estimate. No explanation is provided for these discrepancies with Wittke et al.				

(2013). Due to the uncertain provenience of these ^{14}C samples, we followed Kennett et al. (2015), and did not include any ^{14}C samples for the Lommel YDB in our simulations.				
Melrose, Pennsylvania, United States				
No sources report ^{14}C measurements on samples recovered from the YDB layer.				
Mucuñuque, Venezuela				
No sources report ^{14}C measurements on samples recovered from the YDB layer.				
Murray Springs, Arizona, United States				
A-1045	10,760	100	Charcoal + F_2	Haynes, 2007; Wittke et al., 2013
TX-1045	10,260	140	Humates + F_2	Haynes, 2007
TX-1044	12,600	2440	Charcoal + F_2	Haynes, 2007
TX-1462	10,930	170	Charcoal	Haynes, 2007; Wittke et al., 2013
Discussion				
Wittke et al. (2013) indicate that charcoal sample TX-1462 dates the YDB, but this sample is missing entirely from the narrative, figures, and tables in Kennett et al. (2015). An additional conflict is that TX-1462 is apparently included in their OxCal age-sequence model for Murray Springs (Kennett et al., 2015), despite being absent elsewhere in the text. Further confusion arises from the fact that Wittke et al. (2013) did not include TX-1045 or TX-1044 in their age estimations of the YDB. Of note are several Murray Springs ^{14}C measurements that are incorrectly listed as OSL ages in Wittke et al. (2013): Table S1 (AA-26212, A-1045, and TX-1462). We suspect that this is a typographic error that did not impact their analyses. We deferred to Kennett et al.'s (2015) list of YDB ^{14}C samples for Murray Springs, thereby excluding TX-1462. Given the extreme ^{14}C measurement error for TX-1044, we also excluded this sample in the simulations presented in our main paper. We did, however, include this sample in simulations of an alternative dataset presented in Section 5.				
Ommen, Netherlands				
UCIAMS-46307	11,440	35	Charcoal	Wittke et al., 2013
Discussion				
Kennett et al. (2015) report that no ^{14}C samples were recovered from the Ommen YDB. This conflicts with Wittke et al. (2013), who report that AMS sample UCIAMS-46307 was recovered directly from charcoal in the YDB. Kennett et al. (2015) report that this sample originates from a context stratigraphically below the YDB. For our simulations, we deferred to Kennett et al. (2015) and did not include any samples from Ommen.				
Santa Maira, Spain				
Beta-75225	11,020	140	Charcoal	Aura Tortosa et al., 2008
Discussion				
We followed Kennett et al. (2015) and included this single sample for the Santa Maira YDB.				
Sheriden Cave, Ohio, United States				
UCI-38249-(C)	10,915	30	Bone Clovis point	Waters et al., 2009
Beta-127909	10,840	80	Wood charcoal	Tankersley and Redmond, 1999
Beta-127910	10,960	60	Wood charcoal	Tankersley and Redmond, 1999
Discussion				
Kennett et al. (2015) indicate that all 3 of these samples are associated with the YDB at Sheriden Cave, which is visible as a discontinuous ash layer. We have included all 3 measurements in our simulations.				
Talega, California, United States				
Beta-196150	11,070	50	Charcoal	Bergin, 2011 in Kennett et al., 2015; Wittke et al., 2013
Discussion				
We followed Kennett et al. (2015) and included this single sample for the Talega YDB.				
Topper, South Carolina, United States				
AA-100294	10,958	65	Charcoal	Goodyear, 2013
Goodyear (2013) provides one ^{14}C sample from charcoal associated with the Clovis layer at Topper. Wittke et al. (2013) define the YDB as immediately above the Clovis layer from which this date derived. We deferred to Kennett et al. (2015) and included this ^{14}C sample in our simulations.				

4.2. LST Sites and ^{14}C Samples

Many of the samples described here were originally summarized in Baales et al. (2002). Three rows highlighted in orange describe ^{14}C samples recovered from within the LST and summarized by Baales et al. (2002) yet excluded in our simulations for reasons specified in the associated discussion paragraphs. Ten rows highlighted in blue describe ^{14}C samples recovered from stratigraphic contexts near the LST, but not from within it. Since these samples likely do not date the Laacher See volcanic eruption, we excluded them from our simulations.

Laboratory Number	Reported ^{14}C		Material	Original Reference
	μ	σ		
Brohl Valley				
HV-11774	11,075	185	Plant remains	Heine, 1993
HD-17900	11,277	26	Tree 1/4, rings 1–38	Kromer et al., 1998
KN-3800	11,240	100	Populus	Street, 1993
KN-3801	11,260	95	Populus	Street, 1993
KN-3802	11,280	100	Populus	Street, 1993
KN-3803	11,510	90	Populus	Street, 1993
Unknown	11,085	90	Charcoal	Frechen, 1952; Schweitzer, 1958
HD-17100	11,206	20	1a ca. 50 rings	Kromer et al., 1998
HD-17145	11,223	22	3a ca. 50 rings	Kromer et al., 1998
HD-17101	11,121	28	5b ca. 50 rings	Kromer et al., 1998
Discussion				
Neither Frechen (1952) nor Schweitzer (1958) report the laboratory number for the unknown sample.				
Glees				
GrA-?	10,680	85	Charcoal	Frechen, 1959; Schweitzer, 1958
Discussion				
Originally reported by Schweitzer (1958). Frechen (1959) provides the laboratory but not the sample number.				
Kruft				
HD-19098	11,063	30	Populus 9 rings 1-20	Baales et al., 1998; Kromer et al., 1998
HD-18438	11,065	22	Populus 8 outer rings	Baales et al., 1998; Kromer et al., 1998
HD-19092	11,066	28	Populus 9 rings 21-30	Baales et al., 1998; Kromer et al., 1998
HD-18622	11,073	33	Populus 9 rings 31-40	Baales et al., 1998; Kromer et al., 1998
HD-19037	11,075	28	Populus 9 rings 41-50	Baales et al., 1998; Kromer et al., 1998
HD-18648	11,037	27	Populus 1 rings 31-40	Baales et al., 1998; Kromer et al., 1998
Discussion				
Four of these measurements (HD-19098, HD-19092, HD-18622, and HD-19037) originate from the same tree (Populus 9). For this reason, we only included the sample corresponding to rings 1-20 (HD-19098) in our simulation. This sample logically corresponds to the only Populus 9 measurement that could plausibly date the calendar year of the Laacher See eruption. The other three samples must precede the eruption it in the order indicated by their ring sequences.				
Miesenhein IV				
OxA-3584	11,190	90	*Alces alces* bone	Hedges et al., 1993

OxA-3585	11,310	95	*Alces alces* bone	Hedges et al., 1993
OxA-3586	11,190	100	*Alces alces* bone	Hedges et al., 1993
Discussion				
Hedges et al. (1993) note that the *Alces* remains predate the Laacher See eruption as there was time for moss accumulation prior to deposition of the LST. While not enough time elapsed to fully surround the remains in the pre-LST layer, the event must necessarily have followed the death of the animal, and we have therefore excluded these measurements.				
Nette Valley				
W-525	10,800	300	Charcoal	Frechen, 1959
N/A	10,880	95	Charcoal	van den Bogaard and Schmincke, 1985
Discussion				
In their supplementary data, van den Bogaard & Schmincke (1985) note that the second ^{14}C measurement is from a personal communication with Geyh in 1976.				
Soppensee				
ETH-5290	10,760	80	Macrofossils	Hajdas et al., 1993, 1995
ETH-6930	11,190	80	Macrofossils	Hajdas et al., 1993, 1995
ETH-6932	10,540	150	Macrofossils	Hajdas et al., 1993, 1995
ETH-12617	11,040	90	Macrofossils and wood/bark	Hajdas et al., 1995
ETH-12615	11,370	90	Macrofossils and wood/bark	Hajdas et al., 1995
ETH-12613	11,220	90	Macrofossils and wood/bark	Hajdas et al., 1995
ETH-12610	11,180	100	Macrofossils and wood/bark	Hajdas et al., 1995
Discussion				
Hajdas et al. (1995) report the bottom four ^{14}C measurements on samples from 1-2 cm sediment slices that also contain ash from the Laacher See eruption. However, the relationship between the sample materials and the ash within each slice is unknown. ETH-5290 and ETH-6930 are from materials "stratigraphically close" to Laacher See ash (Hajdas et al., 1993), although it is unclear how close the ash is to each sample or if the samples originate from within ash. Hajdas et al. (1995) subsequently estimated that ETH-5290 postdates the LST by 20 ^{14}C years and ETH-6930 predates the LST by 60 ^{14}C years. ETH-6932 was originally reported by Hajdas et al. (1993), but they did not describe this sample as associated with Laacher See ash. Hajdas et al. (1995) later estimated that this sample predates the LST by 140 ^{14}C years. Although these measurements all appear to originate from sample organisms that died chronologically near the Laacher See eruption, the exact chronological relationships between each sample and deposition of the LST are unclear. In some cases, samples appear to postdate the LST, which is an issue that our simulations do not account for. As such, we excluded these measurements from our simulations.				
Thelenberg				
HD-?	10,950	190	Charcoal	Frechen, 1959
Discussion				
Frechen (1959) provides the laboratory but not the sample number.				
Tönnisstein				
W-528	11,150	200	Charcoal	Rubin and Alexander, 1960; Street et al., 1994
GrA-?	11,025	90	Charcoal	Frechen, 1959
Discussion				
Frechen (1959) provides the laboratory but not the sample number for the latter sample.				

5. Simulations of Alternative LST_{Obs} and YDB_{Obs}

In total, this "multiverse analysis" entailed 42 separate simulations over six different parameterizations (A1–C1 and A2–C2) and across seven different observed datasets (the main text dataset scored as all AMS measurements, as well as the three alternative datasets, each run both with the reported AMS/GPC/LSC distinctions and with all measurements scored as AMS). When describing the results for each alternative, we focus on simulation C2, much like the results described in the main paper. We focus on simulation C2 because it contains the most sources of variability, which likely most closely approximates the large number of sources that must affect real ^{14}C datasets (i.e., C2 is characterized the most realism of the six simulations). The remaining five simulations show expectations when these sources of variability are excluded (or their effects are relaxed, as is the case for the OWM simulations with λ set to 0.04).

5.1. Alternative 1

The Alternative 1 dataset includes the five measurements that were excluded from simulations in the main text. The $\sigma^{14}C$ and dissimilarity values for both YDB_{Obs} and LST_{Obs} become a more probable outcome across simulations for Alternative 1 (Figure S5.1). However, this change is modest for YDB_{Obs}, which remains a highly improbable event, with less than 0.1% of simulated $\sigma^{14}C$ and dissimilarity values exceeding the observed $\sigma^{14}C$ and dissimilarity values in any given simulation.

Treating all Alternative 1 measurements as AMS decreases the probability of observing a dataset with $\sigma^{14}C$ and dissimilarity values as large as those in either observed dataset. This decrease is largest for LST_{Obs}, which is dominated by non-AMS measurements. Despite the decrease having a disproportionately large effect on the probability of observing $\sigma^{14}C$ and dissimilarity values for LST_{Obs}, the dispersion statistics associated with LST_{Obs} remain orders of magnitude more probable than those associated with YDB_{Obs}.

5.2. Alternative 2

Alternative 2 excludes three YDB_{Obs} measurements with potential reliability issues, which may have artificially increased dispersion in YDB_{Obs}. LST_{Obs} retains all 19 measurements used in the main text for this event. This alternative was designed to be favorable to the Younger Dryas Impact Hypothesis by reducing dispersion in the observed dataset ^{14}C measurements.

While simulated datasets as dispersed as YDB_{Obs} do become more probable when these three measurements are excluded, YDB_{Obs} $\sigma^{14}C$ and dissimilarity values remain highly improbable, with less than 0.5% of iterations producing $\sigma^{14}C$ and dissimilarity values greater than those values for YDB_{Obs} in any simulation (Figure S5.1). The minor LST results differences between the main text and the results presented here are due to simulation variance, given that both simulations used the same set of LST_{Obs} measurements.

Much like Alternative 1, scoring all Alternative 2 measurements as AMS reduces the probability of observing $\sigma^{14}C$ and dissimilarity values as large as those in either observed dataset. However, this reduction is slight for YDB_{Obs}. Although simulated LST $\sigma^{14}C$ and dissimilarity values are more greatly affected by scoring all observed measurements as AMS, the LST_{Obs} $\sigma^{14}C$ and dissimilarity values remain probable relative to the YDB_{Obs} values, in the context of the simulation.

5.3. Alternative 3

The Alternative 3 dataset excludes 22 measurements from sites that make up a disproportionately large share of YDB_{Obs} and LST_{Obs}. For YDB_{Obs}, these excluded measurements are the samples from Arlington Canyon (*n* = 12), and for LST_{Obs}, these measurements are the samples from Brohl Valley (*n* = 10).

YDB_{Sim} $\sigma^{14}C$ and dissimilarity values exceed YDB_{Obs} $\sigma^{14}C$ and dissimilarity values more often for Alternative 3 than they do for the observed dataset used in the main text, but this gain is slight (Figure S5.1). Even when these Arlington Canyon samples are excluded, simulations produced $\sigma^{14}C$ and dissimilarity values exceeding those values for YDB_{Obs} in no more than 0.1% of iterations. In contrast, when the Brohl Valley measurements are excluded from LST_{Obs}, LST_{Sim} $\sigma^{14}C$ and dissimilarity values more often exceed LST_{Obs} $\sigma^{14}C$ and dissimilarity values. In those simulations that include the LBM, this ranges from 7.5–28.3% of simulated $\sigma^{14}C$ values and 10.0–43.6% of dissimilarity values.

Scoring all Alternative 3 measurements as AMS reduces the number of YDB_{Sim} and LST_{Sim} datasets with $\sigma^{14}C$ and dissimilarity values that exceed those values for YDB_{Obs} and LST_{Obs}. This reduction is greatest for LST measurements in Alternative 3, but even with this larger reduction, the LST_{Obs} $\sigma^{14}C$ and dissimilarity values remain much more probable than do the YDB_{Obs} $\sigma^{14}C$ and dissimilarity values, given simulated expectations for those values.

5.4. Main text LST_{Obs} and YDB_{Obs} measurements scored as entirely AMS

As with the alternative datasets, we also completed the simulation for the main text dataset with all measurements scored as AMS (Figure S5.1). YDB_{Sim} $\sigma^{14}C$ values exceed YDB_{Obs} $\sigma^{14}C$ values slightly more often when all measurements are scored as AMS, while simulated dissimilarity values exceed observed dissimilarity values *less* often. In all cases, the all-AMS YDB simulations produce $\sigma^{14}C$ or dissimilarity values that exceed the observed values in no more than 0.1% of iterations. The number of LST_{Sim} iterations that produced $\sigma^{14}C$ or dissimilarity values exceeding the LST_{Obs} $\sigma^{14}C$ and dissimilarity values decreased as a result of scoring all measurements as AMS, but even with this decrease, the LST_{Obs} $\sigma^{14}C$ and dissimilarity values remain much more probable in the context of the simulation than do the YDB_{Obs} $\sigma^{14}C$ and dissimilarity values.

5.5. Discussion

The alternative simulations demonstrate that inferences from our simulations vary with data inclusion decisions, although the variation that we investigated here does not substantially alter the qualitative inferences presented in the main text: The amount of dispersion in the YDB_{Obs} ^{14}C measurements is highly improbable, given a synchronous event. In contrast, dispersion in the LST_{Obs} ^{14}C measurements, while not highly probable, is orders of magnitude more probable than the dispersion in the YDB_{Obs} measurements, given a synchronous event. This difference is especially interesting for Alternative 2, in which the YDB_{Obs} dissimilarity value is only 0.01 greater than the LST_{Obs} dissimilarity value, and the YDB_{Obs} $\sigma^{14}C$ value falls *below* the LST_{Obs} $\sigma^{14}C$ value. This highlights the context-dependent aspect of these simulations—the degree of clustering in ^{14}C measurements that should be expected depends on many variables associated with those measurements, including their reported measurement error, the number of possible "old wood" samples, the number of laboratories that contributed measurements, and the measurement methods employed by those laboratories. Although the observed $\sigma^{14}C$ and dissimilarity values for Alternative 2 might suggest that the YDB_{Obs} measurements are more consistent with synchroneity than are the LST_{Obs} measurements, aspects of YDB_{Obs} strongly suggest that they should be much more clustered than this if these measurements are associated with a synchronous event.

Inferences also necessarily change given different choices about simulation design, which are theoretically infinite. We designed the simulations to include those variables that should have the largest effects on the dispersion of ^{14}C measurements, but it is possible to imagine arguments for other variables that we excluded, or arguments for different effects associated with the variables that we did include (e.g., the OWM entails choices about which value to specify for λ, as well as the choice to model "old wood" effects with an exponential distribution. See SI Section 6 for further discussion). We aimed to demonstrate a range of inferences given different simulation assumptions, but this range could be further extended with other simulation designs. An important observation for these simulations is that the expected dispersion within a set of synchronous ^{14}C measurements generally declines when fewer sources of variability are considered. This is especially true of the laboratory variability described in the LBM. As such, we largely ignored the implications of the simulations that excluded the LBM, as it is unrealistic to expect a variety of laboratories with different protocols to measure ^{14}C with perfect precision and accuracy. Such a scenario would necessarily underestimate the amount of dispersion expected in set of ^{14}C measurements. This expectation is supported by multiple inter-laboratory ^{14}C measurement studies (Boaretto et al., 2003; International Study Group,1982; Scott et al., 1990, 1998, 2010a; Scott, Cook, Naysmith et al. 2007). We displayed the results from simulations that excluded the LBM to illustrate underestimation effects on $\sigma^{14}C$ and dissimilarity values when this variability is ignored.

In addition to the inclusion or exclusion of the LBM, there is also the issue of choices in specifying the LBM (described in SI Section 3). Much like simulation design choices, the LBM would characterize inter- and intra-laboratory measurement variability differently under alternative specifications. We aimed to include those variables most likely to affect the dispersion of ^{14}C values in this context, although other choices might plausibly be made. For example, rather than model the effect of AMS vs GPC/LSC measurements, one could model the effects of AMS vs GPC vs LSC measurements. We lumped the latter two measurement methods together since there are few data within each measurement method group when GPC/LSC measurements are subdivided into GPC and LSC measurements. A primary measurement distinction commonly drawn by researchers working with ^{14}C datasets is that of AMS compared to earlier counting methods, such as GPC and LSC. As such, we incorporated this distinction into our model.

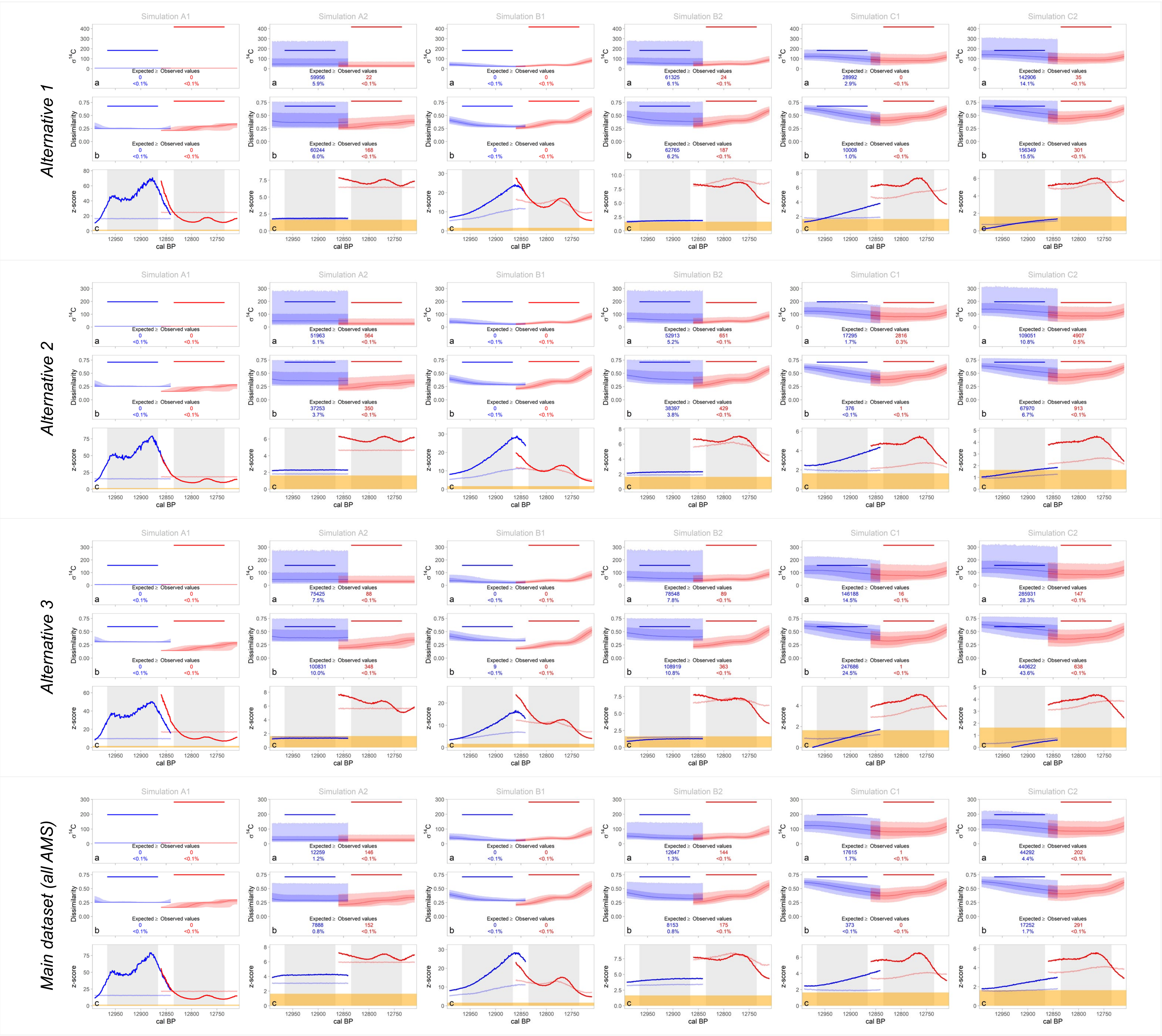

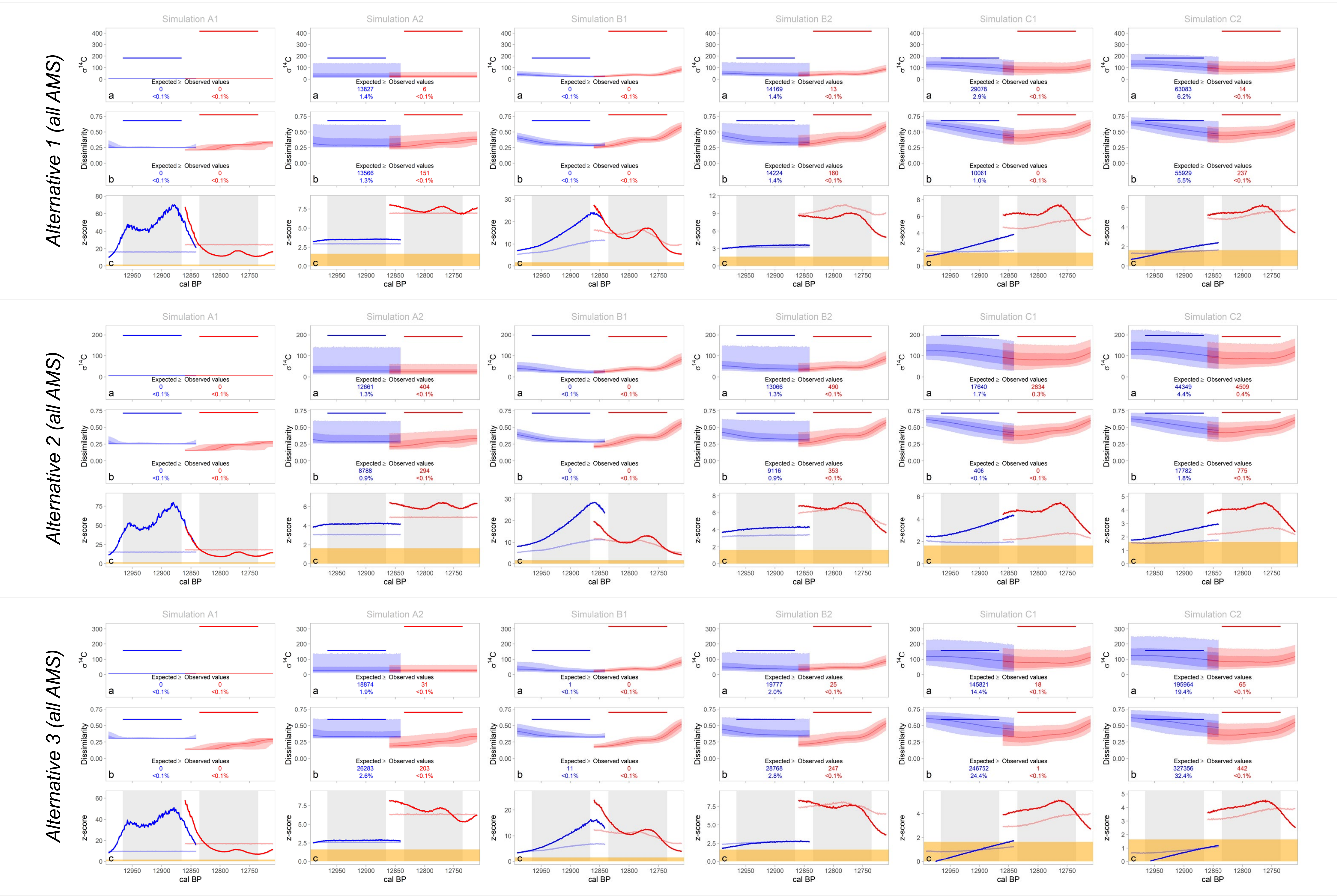

Figure S5.1. Results of simulations over the three alternative datasets, the three alternative datasets scored as all AMS measurements, and the main dataset scored as all AMS measurements. Blue geometry corresponds to LST simulations, and red geometry corresponds to YDB simulations. Refer to Fig. 4 (main text) for interpreting the segments and bands in each panel.

6. Simulations with Alternative Old Wood Model λ Values

In the main paper, simulations were run with old wood offsets drawn from exponential distributions with λ set to 0.04 and 0.01 (mean respective offsets, 25 and 100 years; 95% of respective expected offsets, 0–75 years and 0–300 years) as well as simulations that lacked old wood offsets. Reducing λ allows for larger offsets, increasing dispersion in simulated datasets. In the main paper, we selected λ values with the goal of bounding realistic old wood effects in each context of interest. However, λ values could theoretically be decreased until simulations generate datasets matching or exceeding dispersion in the observed datasets.

We ran additional simulations with reduced λ values to examine what degree of old wood age offsetting would be necessary to obtain the level of dispersion in YDB_{Obs}. These additional simulations set λ to 5.0e-3 and 2.5e-3. For the former λ value, the mean expected age offset is 200 years, with 95% of expected offsets falling within 0–600 years. For the latter λ value, the mean expected age offset is 400 years, with 95% of expected offsets falling within 0–1200 years. These offsets are generally large given the tree species identified in each dataset, and they likely overestimate old wood effects. For these alternative simulations, we used the observed datasets presented in the main paper rather than the various alternative datasets.

At λ = 5.0e-3, simulated dissimilarity and $\sigma^{14}C$ values indicate less dispersion in YDB_{Sim} datasets than in YDB_{Obs} (Figures S6.1 and S6.2). In contrast, LST_{Sim} are roughly as dispersed as LST_{Obs}, suggesting that this magnitude of old wood effects is consistent with a known synchronous event when the average old wood offset is at 200 calendar years. YDB_{Sim} datasets resemble or are more dispersed than YDB_{Obs} when λ = 2.5e-3, although LST_{Sim} datasets are much too dispersed relative to LST_{Obs} (Figures S6.3 and S6.4). This suggests that an average old wood offset between 200 and 400 years is required to produce dispersion in YDB_{Sim} datasets that is comparable to those in YDB_{Obs}.

The effects of old wood offsets begin to swamp those of the LBM as λ decreases, suggesting that laboratory error and repeatability has little explanatory power if YDB_{Obs} truly results from a synchronous event. When λ reaches 2.5e-3, dispersion in YDB_{Obs} falls within two z-scores of the mean dispersion in the simulated datasets, regardless of whether than LBM is included (Figures S6.3 and S6.4). As such, old wood effects must be a proportionally large source of variability in ^{14}C measurements to account for the dispersion in YDB_{Obs}. We find it unrealistic to assume that the “old wood” measurements in this dataset precede the event of interest by an average of 400 years. Rather, a more conservative assumption, given the results, is that a single event was not responsible for YDB_{Obs}.

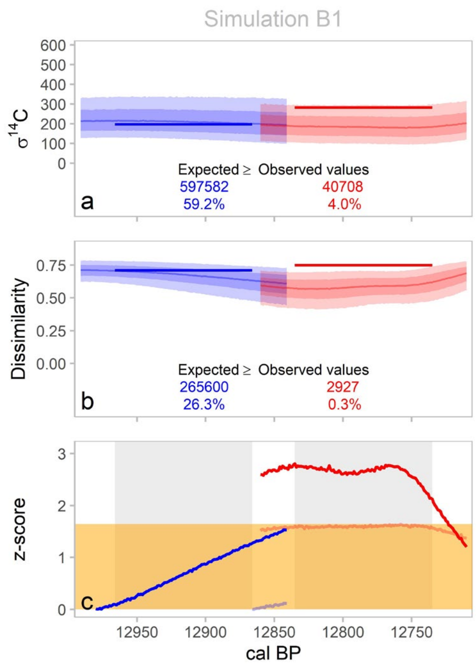

Figure S6.1. Results of simulations with λ = 5.0e-3 and no LBM. Blue geometry corresponds to LST simulations, and red geometry corresponds to YDB simulations. Refer to Fig. 4 (main text) for interpreting the segments and bands in each panel.

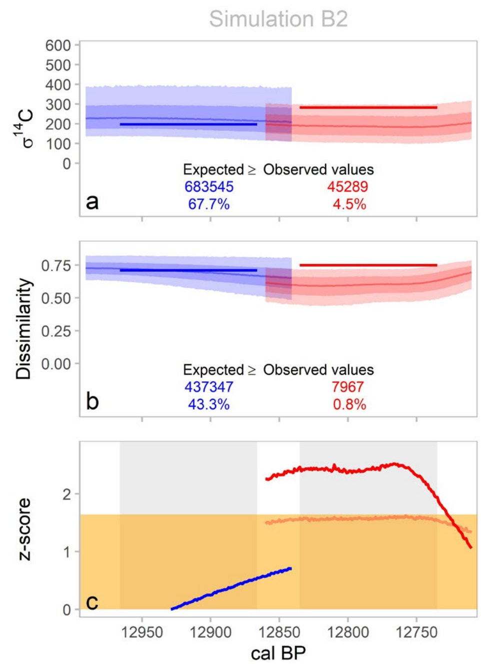

Figure S6.2. Results of simulations with λ = 5.0e-3 and the LBM. Blue geometry corresponds to LST simulations, and red geometry corresponds to YDB simulations. Refer to Fig. 4 (main text) for interpreting the segments and bands in each panel.

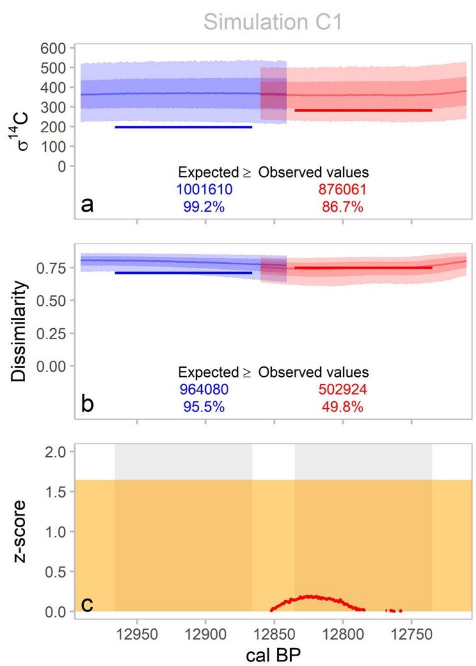

Figure S6.3. Results of simulations with λ = 2.5e-3 and no LBM. Blue geometry corresponds to LST simulations, and red geometry corresponds to YDB simulations. Refer to Fig. 4 (main text) for interpreting the segments and bands in each panel.

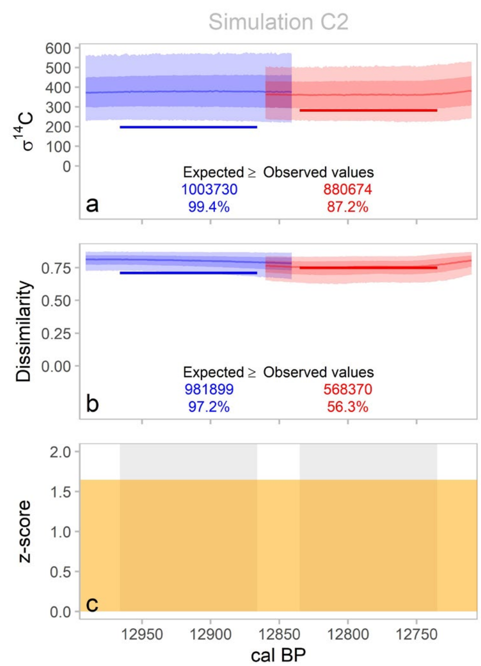

Figure S6.4. Results of simulations with λ = 2.5e-3 and the LBM. Blue geometry corresponds to LST simulations, and red geometry corresponds to YDB simulations. Refer to Fig. 4 (main text) for interpreting the segments and bands in each panel.

7. Sample Size Differences Between YDB_{Obs} and LST_{Obs}

One feature that differs between YDB_{Obs} and LST_{Obs} is the number of measurements in each dataset. There are 30 measurements in YDB_{Obs}, while LST_{Obs} contains only 19 measurements. This raises the question of whether YDB_{Obs} could be more consistent with synchroneity if it was reduced to 19 measurements. Depending on which 19 measurements are subsampled from YDB_{Obs}, a reduced dataset of 19 measurements could be more or less dispersed than the full dataset of 30 measurements.

To understand the implications of differences in sample size, we ran the simulation using three subsampled datasets of 19 YDB_{Obs} measurements. To create these datasets, we first generated 10,000 randomly subsampled datasets from the 30 YDB_{Obs} measurements. We calculated $\sigma^{14}C$ for each dataset, resulting in a distribution of 10,000 $\sigma^{14}C$ values. Next, we selected the datasets associated with the 2.5%, 50.0%, and 97.5% percentile values in the $\sigma^{14}C$ distribution. These represent plausible observed datasets of 19 measurements with low, medium, and high dispersion, given the known dataset of 30 YDB_{Obs} measurements (Tables S7.1 and S7.2).

The subsampled YDB_{Obs} dataset with low dispersion has a dissimilarity value comparable to the dissimilarity value for LST_{Obs}. The YDB_{Obs} $\sigma^{14}C$ value is ~24.5 lower than the $\sigma^{14}C$ value for LST_{Obs}, suggesting an observed YDB dataset that is potentially more consistent with synchroneity than is the observed LST dataset. Despite this, the observed statistics for the low dispersion subsample of YDB_{Obs} are still more dispersed than those expected from the simulations (Figure S7.1). In nearly all versions of the simulation, less than 0.1% of YDB_{Sim} dissimilarity and $\sigma^{14}C$ values are greater than the dissimilarity and $\sigma^{14}C$ values for YDB_{Obs}. The exceptions to this are the $\sigma^{14}C$ values of the C simulations, which have the larger old wood offset ($\lambda = 0.01$). In simulation C1, which excludes the LBM, 1.6% of YDB_{Sim} $\sigma^{14}C$ values exceed the YDB_{Obs} $\sigma^{14}C$ value (Figure S7.1). In simulation C2, which includes the LBM, 2% of YDB_{Sim} $\sigma^{14}C$ values exceed the YDB_{Obs} $\sigma^{14}C$ value. Although these percentages are larger than those obtained from using the full 30 measurements in YDB_{Obs}, they are still low, especially compared to the LST simulations.

The subsampled YDB_{Obs} dataset with medium dispersion has dissimilarity and $\sigma^{14}C$ values similar to those obtained for the YDB_{Obs} dataset with the full 30 measurements. As such, the simulated results resemble those presented for the full dataset in the main text (Figure S7.1). As expected, the subsampled YDB_{Obs} dataset with high dispersion is extremely inconsistent with the simulated datasets (Figure S7.1).

Results demonstrate that despite the sample size differences between LST_{Obs} (n = 19) and YDB_{Obs} (n = 30), it is highly improbable that a YDB_{Obs} dataset that has been rarefied to 19 measurements would be consistent with synchroneity. Although the low dispersion subsample is *more* consistent with synchroneity than is the full YDB_{Obs} dataset of 30 measurements, it remains a highly improbable outcome, given a synchronous event.

Table S7.1. Dispersion in subsampled YDB_{Obs} measurements.

	Dispersion in subsampled YDB_{Obs} datasets		
	Low	Medium	High
$\sigma^{14}C$	172.45	277.78	343.85
Dissimilarity	0.71	0.73	0.83

Table S7.2. YDB_{Obs} measurements retained in each subsample (marked with 'X's). Alphabetical site IDs correspond to Fig. 1 and Table 1 in the main text.

Site ID: ^{14}C Measurement	Material	AMS	OWM sample	YDB_{Obs} dispersion Low	Med.	High
G: 11,070 ± 40 (UCIAMS-105429)	Charcoal	1	1			X
H: 11,105 ± 30 (UCIAMS-47239)	Charcoal	1	1	X		X
H: 11,095 ± 25 (UCIAMS-36308)	Wood	1	1		X	X
H: 11,095 ± 25 (UCIAMS-42816)	Wood	1	1	X	X	
H: 11,070 ± 25 (UCIAMS-36307)	Wood	1	1	X	X	
H: 11,440 ± 90 (UCIAMS-36961)	Carbon elongate	1	0		X	X
H: 11,185 ± 30 (UCIAMS-36960)	Carbon spherule	1	0	X		X
H: 11,110 ± 35 (UCIAMS-36962)	Wood	1	1	X		X
H: 11,075 ± 30 (UCIAMS-36959)	Glassy carbon	1	0	X		
H: 10,860 ± 70 (Beta-161032)	Charcoal	1	1	X	X	
H: 11,375 ± 25 (UCIAMS-36306)	Wood	1	1			X
H: 11,235 ± 25 (UCIAMS-36305)	Wood	1	1	X	X	X
H: 11,020 ± 25 (UCIAMS-36304)	Wood	1	1			X
K: 10,840 ± 75 (GrA-49524)	Charcoal	1	1	X	X	
K: 10,865 ± 55 (GrA-49509)	Charcoal	1	1	X	X	
K: 11,020 ± 75 (GrA-49515)	Charcoal	1	1		X	
I: 11,900 ± 80 (AA-27486)	Charcoal	1	1		X	X
I: 10,710 ± 85 (AA-26654)	Charcoal	1	1	X	X	X
J: 11,070 ± 60 (Beta-184854)	Sed. organics	1	0	X	X	X
O: 10,760 ± 100 (A-1045)	Charcoal	0	1	X	X	X
O: 10,260 ± 140 (TX-1045)	Humates	0	0			X
Q: 10,915 ± 30 (UCI-38249)	Bone Clovis point	1	0	X	X	X
Q: 10,840 ± 80 (Beta-127909)	Wood charcoal	1	1	X	X	X
Q: 10,960 ± 60 (Beta-127910)	Wood charcoal	1	1	X		
L: 10,610 ± 25 (UCIAMS-29317)	Charcoal	1	1	X		X
M: 10,780 ± 135 (I-141)	Charcoal	0	1	X	X	
N: 10,870 ± 40 (Beta-369246)	Charcoal	1	1		X	
R: 11,070 ± 50 (Beta-196150)	Charcoal	1	1		X	
S: 10,958 ± 65 (AA-100294)	Charcoal	1	1		X	X
P: 11,020 ± 140 (Beta-75225)	charcoal	1	1	X		X

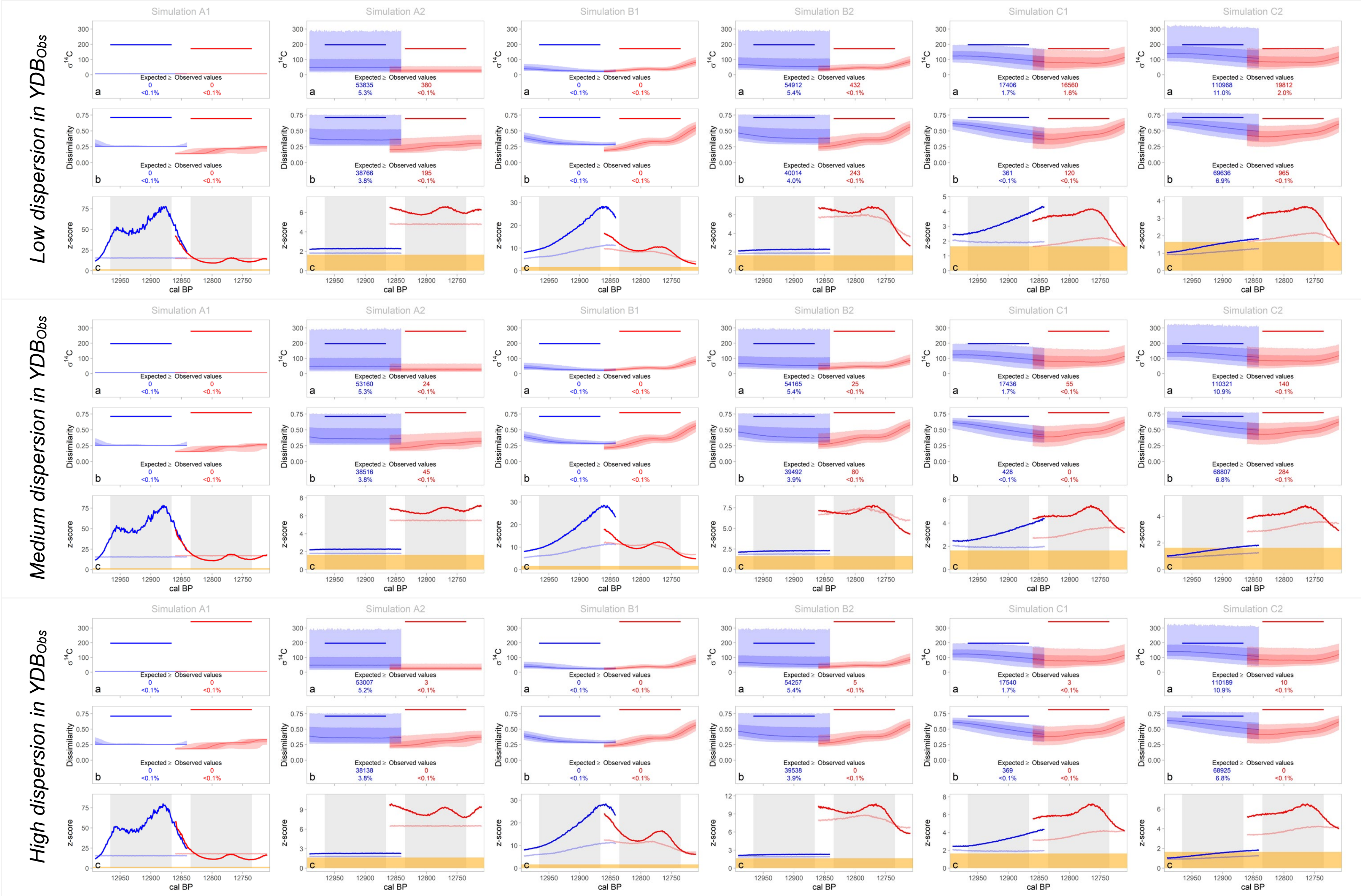

Figure S7.1. Results of simulations with YDB_{Obs} subsampled to 19 measurements. Blue geometry corresponds to LST simulations, and red geometry corresponds to YDB simulations. Refer to Fig. 4 (main text) for interpreting the segments and bands in each panel.

8. References for Supplemental Information Appendix

Aura Tortosa, J.E., Miret i Estruch, C., Morales Pérez, J.V., 2008. Coves de Santa Maira (Castell de Castells, La Marina Alta, Alacant). Campaña de 2008. *Saguntum, PLAV* 40, 227–232.

Baales, M., Bittmann, F., Kromer, B., 1998. Verkohlte Bäume im Trass der Laacher See-Tephra bei Kruft (Neuwieder Becken): Ein Beitrag zur Datierung des Laacher See-Ereignisses und zur Vegetation der Allerød-Zeit am Mittelrhein. *Archäologisches Korrespondenzblatt* 28, 191–204.

Baales, M., Jöris, O., Street, M., Bittmann, F., Weninger, B., Wiethold, J., 2002. Impact of the Late Glacial Eruption of the Laacher See Volcano, Central Rhineland, Germany. *Quaternary Research* 58, 273–288.

Bement, L.C., Madden, A.S., Carter, B.J., Simms, A.R., Swindle, A.L., Alexander, H.M., Fine, S., Benamara, M., 2014. Quantifying the distribution of nanodiamonds in pre-Younger Dryas to recent age deposits along Bull Creek, Oklahoma Panhandle, USA. *Proceedings of the National Academy of Sciences USA* 111, 1726–1731. https://doi.org/10.1073/pnas.1309734111

Bengtsson, H., Bravo, H.C., Gentleman, R., Hossjer, O., Jaffee, H., Jian, D., Langfelder, P., Hickey, P., 2018. matrixStats: Functions that Apply to Rows and Columns of Matrices (and to Vectors).

Bergin, K.A., 2011. The Archaeology of the Talega Site (CA-ORA-907), Orange County, California: Perspective on the Prehistory of Southern California. Viejo California Associates, Mission Viejo. Prepared for the District of the US Army Corps of Engineers, Los Angeles.

Bevan, A., Crema, E.R., 2018. rcarbon v1.2.0: Methods for calibrating and analyzing radiocarbon dates.

Boaretto, E., Bryant, C., Carmi, I., Cook, G., Gulliksen, S., Harkness, D., Heinemeier, J., McClure, J., McGee, E., Naysmith, P., 2003. How reliable are radiocarbon laboratories? A report on the Fourth International Radiocarbon Inter-comparison (FIRI)(1998–2001). *Antiquity* 77, 146–154.

Bunch, T.E., Hermes, R.E., Moore, A.M.T., Kennett, D.J., Weaver, J.C., Wittke, J.H., DeCarli, P.S., Bischoff, J.L., Hillman, G.C., Howard, G.A., Kimbel, D.R., Kletetschka, G., Lipo, C.P., Sakai, S., Revay, Z., West, A., Firestone, R.B., Kennett, J.P., 2012. Very high-temperature impact melt products as evidence for cosmic airbursts and impacts 12,900 years ago. *Proceedings of the National Academy of Sciences USA* 109, E1903–E1912.

Caudullo, G., de Rigo, D., 2016. *Populus tremula* in Europe: distribution, habitat, usage and threats, in: San-Miguel-Ayanz, J., de Rigo, D., Caudullo, G., Houston, T., Mauri, A. (Eds.), *European Atlas of Forest Tree Species*. Publication Office of the European Union, Luxembourg, pp. 138–139.

Firestone, R.B., West, A., Kennett, J.P., Becker, L., Bunch, T.E., Revay, Z.S., Schultz, P.H., Belgya, T., Kennett, D.J., Erlandson, J.M., Dickenson, O.J., Goodyear, A.C., Harris, R.S., Howard, G.A., Kloosterman, J.B., Lechler, P., Mayewski, P.A., Montgomery, J., Poreda, R., Darrah, T., Hee, S.S.Q., Smith, A.R., Stich, A., Topping, W., Wittke, J.H., Wolbach, W.S., 2007. Evidence for an extraterrestrial impact 12,900 years ago that contributed to the megafaunal extinctions and the Younger Dryas cooling. *Proceedings of the National Academy of Sciences USA* 104, 16016–16021.

Frechen, J., 1952. Die Herkunft der spätglazialen Bimstuffe in mittel-und süddeutschen Mooren. *Geologisches Jahrbuch* 67, 209–230.

Frechen, J., 1959. Die Tuffe des Laacher Vulkangebietes als quartärgeologische Leitgesteine und Zeitmarken. *Fortschritte der Geologie in Rheinland und Westfalen* 4, 363–70.

Goodyear, A.C., 2013. Update on the 2012–2013 activities of the Southeastern Paleoamerican Survey. *Legacy* 17, 10–12.
Hajdas, I., Ivy, S.D., Beer, J., Bonani, G., Imboden, D., Lotted, A.F., Sturm, M., Suter, M., 1993. AMS radiocarbon dating and varve chronology of Lake Soppensee: 6000 to 12000 14C years BP. *Climate Dynamics* 9, 107–116.
Hajdas, I., Ivy-Ochs, S.D., Bonani, G., Loiter, A.F., Zolitschka, B., Schlüchter, C., 1995. Radiocarbon age of the Laacher See tephra: 11,230 ± 40 BP. *Radiocarbon* 37, 149–154.
Hajic, E.R., Mandel, R.D., Ray, J.H., Lopinot, N.H., 2007. Geoarchaeology of stratified Paleoindian deposits at the Big Eddy site, Southwest Missouri, U.S.A. *Geoarchaeology* 22, 891–934.
Haynes, C.V., 2007. Radiocarbon dating at Murray Springs and Curry Draw, in: Haynes, C.V., Huckell, B.B. (Eds.), *Murray Springs: A Clovis Site with Multiple Activity Areas in the San Pedro Valley, Arizona*. University of Arizona Press, pp. 229–239.
Haynes, V., Agogino, G., 1960. *Geological Significance of a New Radiocarbon Date from the Lindenmeier Site*. Denver Museum of Natural History Proceedings No. 9. Denver Museum of Natural History.
Hedges, R.E.M., Housley, R.A., Ramsey, C.B., Klinken, G.J.V., 1993. Radiocarbon dates from the Oxford AMS system: Archaeometry Datelist 16. *Archaeometry* 35, 147–167.
Heine, K., 1993. Warmzeitliche Bodenbildung im Bölling/Alleröd im Mittelrheingebiet. *Decheniana* 146, 315–324.
International Study Group, 1982. An inter-laboratory comparison of radiocarbon measurements in tree rings. *Nature* 298, 619–623.
Johnson, E., Holliday, V.T., 1997. Analysis of Paleoindian bonebeds at the Clovis Site: New data from old excavations. *Plains Anthropologist* 42, 329–352.
Kennett, D., Kennett, J., West, G., Erlandson, J., Johnson, J., Hendy, I., West, A., Culleton, B., Jones, T., Staffordjr, T., 2008. Wildfire and abrupt ecosystem disruption on California's Northern Channel Islands at the Ållerød–Younger Dryas boundary (13.0–12.9ka). *Quaternary Science Reviews* 27, 2530–2545.
Kennett, J.P., Kennett, D.J., Culleton, B.J., Aura Tortosa, J.E., Bischoff, J.L., Bunch, T.E., Daniel, I.R., Erlandson, J.M., Ferraro, D., Firestone, R.B., Goodyear, A.C., Israde-Alcántara, I., Johnson, J.R., Jordá Pardo, J.F., Kimbel, D.R., LeCompte, M.A., Lopinot, N.H., Mahaney, W.C., Moore, A.M.T., Moore, C.R., Ray, J.H., Stafford, T.W., Tankersley, K.B., Wittke, J.H., Wolbach, W.S., West, A., 2015. Bayesian chronological analyses consistent with synchronous age of 12,835–12,735 Cal B.P. for Younger Dryas boundary on four continents. *Proceedings of the National Academy of Sciences USA* 112, E4344–E4353.
Kinzie, C.R., Que Hee, S.S., Stich, A., Tague, K.A., Mercer, C., Razink, J.J., Kennett, D.J., DeCarli, P.S., Bunch, T.E., Wittke, J.H., Israde-Alcántara, I., Bischoff, J.L., Goodyear, A.C., Tankersley, K.B., Kimbel, D.R., Culleton, B.J., Erlandson, J.M., Stafford, T.W., Kloosterman, J.B., Moore, A.M.T., Firestone, R.B., Aura Tortosa, J.E., Jordá Pardo, J.F., West, A., Kennett, J.P., Wolbach, W.S., 2014. Nanodiamond-Rich Layer across Three Continents Consistent with Major Cosmic Impact at 12,800 Cal BP. *Journal of Geology* 122, 475–506.
Kromer, B., Spurk, M., Remmele, S., Barbetti, M., Joniello, V., 1998. Segments of Atmospheric 14C Change as Derived from Late Glacial and Early Holocene Floating Tree-Ring Series. *Radiocarbon* 40, 351–358. https://doi.org/10.1017/S0033822200018221
Lopinot, N.H., Ray, J.H., Conner, M.D., 1998. T*he 1997 Excavations at the Big Eddy Site (23CE426) in Southwest Missouri*. Southwest Missouri State University, Springfield, Missouri.
Lopinot, N.H., Ray, J.H., Connor, M.D., 2000. *The 1999 Excavations at the Big Eddy Site (23CE426)*. Center for Archaeological Research Special Publication. Southwest Missouri State University, Springfield, Missouri.

McDonald, L., Chivall, D., Miles, D., Bronk Ramsey, C., 2019. Seasonal variations in the ^{14}C content of tree rings: Influences on radiocarbon calibration and single-year curve construction. *Radiocarbon* 61, 185–194.
McElreath, R., 2017. rethinking v1.59: Statistical Rethinking book package.
Moore, A.M.T., Hillman, G.C., Legge, A.J., Huxtable, J., 2000. *Village on the Euphrates: from Foraging to Farming at Abu Hureyra*. Oxford University Press, Oxford.
Pedersen, T.L., 2018. patchwork: The Composer of ggplots.
R Core Team, 2018. R: A language and environment for statistical computing. R Foundation for Statistical Computing, Vienna, Austria.
Reimer, P.J., Bard, E., Bayliss, A., Beck, J.W., Blackwell, P.G., Ramsey, C.B., Buck, C.E., Cheng, H., Edwards, R.L., Friedrich, M., 2013. IntCal13 and Marine13 radiocarbon age calibration curves 0–50,000 years cal BP. *Radiocarbon* 55, 1869–1887.
Rubin, M., Alexander, C., 1960. U. S. Geological Survey radiocarbon dates V. *Radiocarbon* 2, 129–185.
Schweitzer, H.-J., 1958. Entstehung und Flora des Trasses im nördlichen Laachersee-Gebiet. *E&G Quaternary Science Journal* 9, 28–48.
Scott, E.M., Aitchison, T.C., Harkness, D.D., Cook, G.T., Baxter, M.S., 1990. An Overview of All Three Stages of the International Radiocarbon Intercomparison. *Radiocarbon* 32, 309–319.
Scott, E.M., Cook, G.T., Naysmith, P., 2010a. The Fifth International Radiocarbon Intercomparison (VIRI): An assessment of laboratory performance in Stage 3. *Radiocarbon* 52, 859–865.
Scott, E.M., Cook, G.T., Naysmith, P., 2010b. A report on Phase 2 of the Fifth International Radiocarbon Intercomparison (VIRI). *Radiocarbon* 52, 846–858.
Scott, E.M., Cook, G.T., Naysmith, P., 2007. Error and uncertainty in radiocarbon measurements. Radiocarbon 49, 427–440.
Scott, E.M., Cook, G.T., Naysmith, P., Bryant, C., O'Donnell, D., 2007. A report on Phase 1 of the 5th International Radiocarbon Intercomparison (VIRI). *Radiocarbon* 49, 409–426.
Scott, E.M., Harkness, D.D., Cook, Gt., 1998. Interlaboratory comparisons: lessons learned. *Radiocarbon* 40, 331–340.
Stan Development Team, 2018. RStan 2.17.2: The R interface for Stan.
Street, M.J., 1993. *Analysis of Late Palaeolithic and Mesolithic Faunal Assemblages in the Northern Rhineland, Germany* (Ph.D. dissertation). University of Birmingham.
Tankersley, K.B., Redmond, B.G., 1999. Radiocarbon dating of a Paleoindian projectile point from Sheriden Cave, Ohio. *Current Research in the Pleistocene* 16, 76–77.
van den Bogaard, P., Schmincke, H.-U., 1985. Laacher See Tephra: A widespread isochronous late Quaternary tephra layer in central and northern Europe. *Geological Society of America Bulletin* 96, 1554.
van Geel, P., Coope, G.R., van der Hammen, T., 1989. Palaeoecology and stratigraphy of the late glacial type section at Usselo (The Netherlands). *Review of Paleobotany and Palynology* 60, 25–129.
van Hoesel, A., Hoek, W.Z., Braadbaart, F., van der Plicht, J., Pennock, G.M., Drury, M.R., 2012. Nanodiamonds and wildfire evidence in the Usselo horizon postdate the Allerød-Younger Dryas boundary. *Proceedings of the National Academy of Sciences USA* 109, 7648–7653.
von Wühlisch, G., 2009. *EUFORGEN Technical Guidelines for genetic conservation and use for Eurasian aspen (Populus tremula)*. Biodiversity International, Rome.
Walton, A., Trautman, M.A., Friend, J.P., 1961. Isotopes, Inc. Radiocarbon Measurements I. *Radiocarbon* 3, 47–59.
Waters, M.R., Stafford, T.W., Redmond, B.G., Tankersley, K.B., 2009. The age of the Paleoindian assemblage at Sheriden Cave, Ohio. *American Antiquity* 74, 107–111.

Wickham, H., 2016. ggplot2: Elegant Graphics for Data Analysis. Springer-Verlag, New York.

Wickham, H., 2007. Reshaping data with the reshape package. *Journal of Statistical Software* 21, 1–20.

Wittke, J.H., Weaver, J.C., Bunch, T.E., Kennett, J.P., Kennett, D.J., Moore, A.M.T., Hillman, G.C., Tankersley, K.B., Goodyear, A.C., Moore, C.R., Daniel, I.R., Ray, J.H., Lopinot, N.H., Ferraro, D., Israde-Alcántara, I., Bischoff, J.L., DeCarli, P.S., Hermes, R.E., Kloosterman, J.B., Revay, Z., Howard, G.A., Kimbel, D.R., Kletetschka, G., Nabelek, L., Lipo, C.P., Sakai, S., West, A., Firestone, R.B., 2013. Evidence for deposition of 10 million tonnes of impact spherules across four continents 12,800 y ago. *Proceedings of the National Academy of Sciences USA*110, E2088–E2097.